JGR Atmospheres

RESEARCH ARTICLE
10.1029/2020JD034501

What Controls the Probability Distribution of Local Wave Activity in the Midlatitudes?

Claire Valva[1,2] **and Noboru Nakamura**[1]

[1]Department of the Geophysical Sciences, University of Chicago, Chicago, IL, USA, [2]Courant Institute of Mathematical Sciences, New York University, New York, NY, USA

Key Points:

- Local wave activity (LWA) measures meandering of the jet stream, large values often linked to disruptions of the jet and extreme weather
- Observed probability distribution of LWA is positively skewed due to nonlinearity in the zonal advection (LWA-zonal wind interaction)
- Frequency of large LWA events increases with slower jet and stronger eddy forcing but it is insensitive to meridional temperature gradient

Correspondence to:
N. Nakamura,
nnn@uchicago.edu

Citation:
Valva, C., & Nakamura, N. (2021). What controls the probability distribution of local wave activity in the midlatitudes? *Journal of Geophysical Research: Atmospheres*, *126*, e2020JD034501. https://doi.org/10.1029/2020JD034501

Received 24 DEC 2020
Accepted 24 JUN 2021

Abstract This paper examines probability distributions of *local wave activity* (LWA), a measure of the jet stream's meander, and factors that control them. The observed column-mean LWA distributions exhibit significant seasonal, interhemispheric, and regional variations but are always positively skewed in the extratropics, and their tail often involves disruptions of the jet stream. A previously derived one-dimensional (1D) traffic flow model driven by observed spectra of transient eddy forcing qualitatively reproduces the shape of the observed LWA distribution. It is shown that the skewed distribution emerges from nonlinearity in the zonal advection of LWA even though the eddy forcing is symmetrically distributed. A slower jet and stronger transient and stationary eddy forcings, when introduced independently, all broaden the LWA distribution and increase the probability of spontaneous jet disruption. A quasigeostrophic two-layer model also simulates skewed LWA distributions in the upper layer. However, in the two-layer model both transient eddy forcing and the jet speed increase with an increasing shear (meridional temperature gradient), and their opposing influence leaves the frequency of jet disruptions insensitive to the vertical shear. When the model's nonlinearity in the zonal flux of potential vorticity is artificially suppressed, it hinders wave-flow interaction and virtually eliminates reversal of the upper-layer zonal wind. The study underscores the importance of nonlinearity in the zonal transmission of Rossby waves to the frequency of jet disruptions and associated weather anomalies.

Plain Language Summary Midlatitude weather is characterized by mobile cyclones and anticyclones that cause meandering of the jet stream (transient Rossby waves) in the upper troposphere. The degree of the jet's meander is related to the severity of weather anomaly. Here we use a fluid dynamical metric called *local wave activity* (LWA) to quantify the waviness of the jet stream, or the amplitude of the Rossby waves. Probability distribution of LWA is positively skewed, that is, the jet is modestly wavy most of the time yet there are less frequent but very wavy conditions that disrupt the jet stream regionally. Using theory and idealized numerical models we show that these very wavy conditions arise from mutual reinforcement between the meander of the jet stream and weakening of its eastward wind. It is also found that a slower jet stream and stronger eddy forcing both increase the probability of the jet disruption events, but the probability of such events is insensitive to the pole-to-equator temperature gradient.

1. Introduction

Weather and climate in Earth's midlatitudes are strongly influenced by the behavior of the jet stream. Mobile cyclones and anticyclones cause the jet stream to meander over thousands of kilometers and drive fluctuations in air temperature, wind directions and precipitation at surface. Persistent meandering of the jet stream can disrupt the normal passages of these weather systems and bring about anomalous and extreme weather events in the midlatitudes such as heat waves (Woollings et al., 2018, and refs therein).

As a way to gauge the frequency of anomalous meandering of the jet stream, here we study probability distributions of *local wave activity* (LWA) in the midlatitudes and factors that control them. LWA is defined as latitudinal displacement of quasigeostrophic potential vorticity (QGPV) from a zonally uniform reference state (Huang & Nakamura, 2016, 2017, hereafter HN16 and HN17; see also Equations 3 and 4 below). Since material undulation of QGPV is the essence of Rossby waves, LWA is a fundamental measure of the amplitude of Rossby waves traveling along the jet stream and hence its meandering. Compared to more traditional metrics such as geopotential height anomaly or eddy kinetic energy, LWA obeys a relatively simple budget

that is evaluable from data (HN16, HN17, Ghinassi et al., 2020). Furthermore, LWA is known to covary negatively with the zonal wind along the latitude circle: the wavier the jet, the slower its eastward component (HN16, Nakamura & Huang, 2017, 2018, hereafter NH17 and NH18). This permits an explicit description of nonlinearity associated with eddy-jet interaction, which has been suggested to play an important role for the formation of cold-season blocks in the Northern Hemisphere (e.g., Colucci, 1985; Luo et al., 2019; Mullen, 1987; Nakamura, 1994; Naoe et al., 1997). Disruption of the jet stream often coincides with a large LWA event and a similarly diminished (or reversed) zonal wind on a regional scale (HN16, NH17, NH18). Such condition occurs preferentially in regions where forced stationary waves impose diffluence in the jet stream (Colucci, 2001; Luo, 2005; Paradise et al., 2019; Narinesingh et al., 2020).

As we will see, the observed probability distributions of column LWA are positively skewed, with a tail associated with large wave events that often disrupt the jet stream. We will then demonstrate that simple models like a stochastically forced 1D traffic flow model (Paradise et al., 2019, hereafter P19) and a quasigeostrophic two-layer model reproduce qualitatively the observed LWA distributions. By varying the parameters of the models, we seek to identify factors that control the LWA distribution, particularly its tail end. These parameters include the strength of nonlinearity, overall speed of the jet, transient and stationary eddy forcing, and background baroclinicity (vertical shear). The next section briefly reviews the definition of LWA and its conservation properties. Section 3 surveys the observed climatology and probability distributions of LWA. Section 4 examines the relative roles of gradients and displacements of QGPV in the LWA distributions. In Section 5 we compare the LWA distribution predicted by the 1D model with observations. Results from the two-layer model are discussed in Section 6, followed by concluding remarks in Section 7.

2. Diagnostic Formalism

Large-scale circulation of the midlatitude atmosphere is approximately governed by the quasigeostrophic dynamics. Meandering of the jet stream arises from the meridional displacement of QGPV, q, evaluated in this study as

$$q(\lambda,\phi,z,t) = \zeta + f\left(1 + e^{z/H}\frac{\partial}{\partial z}\left(\frac{e^{-z/H}(\theta-\tilde{\theta})}{\partial\tilde{\theta}\,/\,\partial z}\right)\right), \tag{1}$$

where $f = 2\Omega\sin\phi$ and

$$\zeta = \frac{1}{a\cos\phi}\left(\frac{\partial v}{\partial\lambda} - \frac{\partial(u\cos\phi)}{\partial\phi}\right). \tag{2}$$

In the above (λ,ϕ,z,t) denote longitude, latitude, pressure pseudoheight and time; a and Ω are the Earth's radius and angular velocity; (u,v) are the zonal and latitudinal wind velocities; θ is potential temperature and $\tilde{\theta}(z,t)$ is its hemispheric mean; and H is a constant scale height. We evaluate $\tilde{\theta}$ with instantaneous data, but the time dependence of $\partial\tilde{\theta}\,/\,\partial z$ is very weak, consistent with the quasigeostrophic theory.

We measure the meridional displacement of QGPV with respect to a wave-free, zonally symmetric *reference state* QGPV, $q_{\mathrm{REF}}(\phi,z,t)$. q_{REF} is obtained by an area-preserving "zonalization" of the instantaneous QGPV contours and it is by construction a monotonic function of latitude [See Nakamura and Solomon (2010) and Supporting Information of HN17 and NH18 for the computation method for q_{REF}].

LWA is defined as a zeroth moment of QGPV displaced relative to q_{REF} (HN16, HN17):

$$A(\lambda,\phi,z,t)\cos\phi \equiv -a\int_0^{\Delta\phi} q_e(\lambda,\phi+\phi',z,t)\cos(\phi+\phi')d\phi', \quad \phi'\in[0,\Delta\phi], \tag{3}$$

$$q_e(\lambda,\phi+\phi',z,t) = q(\lambda,\phi+\phi',z,t) - q_{\mathrm{REF}}(\phi,z,t), \tag{4}$$

where $\phi+\Delta\phi(\lambda,\phi,z,t)$ is the latitude at which the displaced contour of $q = q_{\mathrm{REF}}(\phi,z,t)$ is located. Since LWA involves the line integral of QGPV, it carries a dimension of velocity (ms^{-1}). Since $q_e \le 0$ where $0 \le \phi' \le \Delta\phi$ and $q_e \ge 0$ where $\Delta\phi \le \phi' \le 0$, A is always nonnegative.

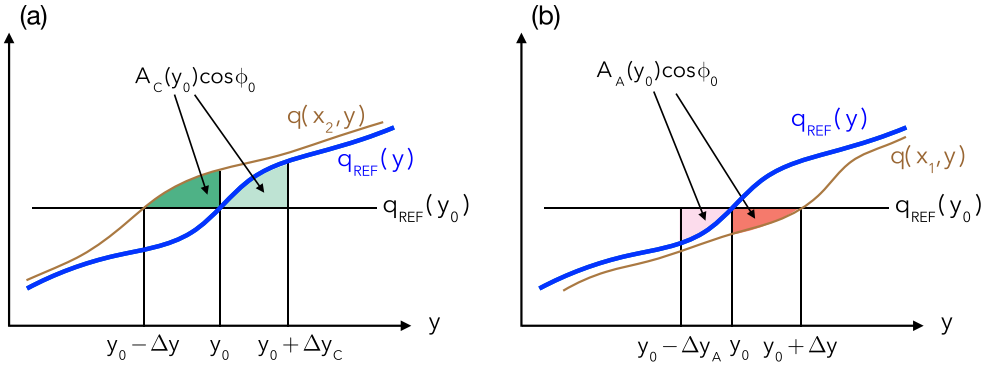

Figure 1. Schematic of cyclonic and anticyclonic local wave activity (LWA) at a particular longitude. Horizontal axis is latitude $\left(y \equiv a\sin\phi\right)$. (a) quasigeostrophic potential vorticity (QGPV) (brown curve) is displaced equatorward relative to q_{REF} (blue curve). The area of dark green shading equals $A_{\mathrm{C}}\cos\phi$ at $y = y_0$ (Equation 6). The bounding latitude of lightly shaded area defines $y_0 + \Delta y_{\mathrm{C}}$, where the two shaded regions have identical area (Equation 8). (b) Same as (a) but for poleward displacement of QGPV. The red area equals $A_{\mathrm{A}}\cos\phi$ at $y = y_0$ and $y_0 - \Delta y_{\mathrm{A}}$ defines the bounding latitude of the lightly shaded area (Equations 7 and 9). See text for details.

As suggested by Chen et al. (2015), LWA may be further partitioned into cyclonic and anticyclonic contributions, A_{C} and A_{A}:

$$A(\lambda,\phi,z,t)\cos\phi = \left[A_{\mathrm{C}}(\lambda,\phi,z,t) + A_{\mathrm{A}}(\lambda,\phi,z,t)\right]\cos\phi, \tag{5}$$

$$A_{\mathrm{C}}\cos\phi \equiv a\int_{-\Delta\phi}^{0} q_e(\lambda,\phi+\phi',z,t)\cos(\phi+\phi')d\phi', \quad -\Delta\phi \le \phi' \le 0 \text{ and } q_e \ge 0, \tag{6}$$

$$A_{\mathrm{A}}\cos\phi \equiv -a\int_{0}^{\Delta\phi} q_e(\lambda,\phi+\phi',z,t)\cos(\phi+\phi')d\phi', \quad 0 \le \phi' \le \Delta\phi \text{ and } q_e \le 0, \tag{7}$$

Figure 1 illustrates the evaluation of Equations 6 and 7. Suppose at one longitude QGPV is displaced equatorward relative to q_{REF} (Figure 1a). The displacement from $y = y_0$ $(\equiv a\sin\phi_0)$ is $-\Delta y = a[\sin(\phi_0 - \Delta\phi) - \sin\phi_0]$. Cyclonic LWA $A_{\mathrm{C}}\cos\phi_0$ is then given by the area of dark green shading. At another longitude QGPV is displaced poleward (Figure 1b), in which case anticyclonic LWA $A_{\mathrm{A}}\cos\phi$ is given by the area of red shading. Note that equatorward and poleward displacements can be detected simultaneously at the same longitude if the QGPV contour is overturned (see Figure 1b of HN16). By construction A_{C} and A_{A} are both nonnegative, but their definitions are reversed in the Southern Hemisphere (SH) such that A_{C} (A_{A}) is always associated with equatorward (poleward) displacement.

After obtaining LWA we find "backward displacements," $\Delta\phi_C$ and $\Delta\phi_A$, by rewriting LWA as

$$A_{\mathrm{C}}\cos\phi = a\int_{0}^{\Delta\phi_C}\left[q_{\mathrm{REF}}(\phi+\phi') - q_{\mathrm{REF}}(\phi)\right]\cos(\phi+\phi')d\phi', \qquad 0 \le \phi' \le \Delta\phi_c, \tag{8}$$

$$A_{\mathrm{A}}\cos\phi = a\int_{-\Delta\phi_A}^{0}\left[q_{\mathrm{REF}}(\phi) - q_{\mathrm{REF}}(\phi+\phi')\right]\cos(\phi+\phi')d\phi', \qquad -\Delta\phi_A \le \phi' \le 0. \tag{9}$$

This amounts to finding the bounding latitudes of the lightly shaded regions in Figure 1, whose areas are identical with those with darker shade. Unlike $\Delta\phi$ in Equations 6 and 7, which merely marks the location of the displaced QGPV contour, $\Delta\phi_{\mathrm{C}}$ and $\Delta\phi_{\mathrm{A}}$ quantify the required displacements of the reference-state QGPV to create the observed wave activity. Thus, Equations 8 and 9 cast LWA as a function of q_{REF} and displacement, and in particular establish a one-to-one relationship between LWA and displacement because q_{REF} is a monotonic function of latitude (see Section 4). In the small-amplitude limit, the shaded areas in Figure 1 are approximately triangles and therefore $A_{\mathrm{C}}\cos\phi_0$ and $A_{\mathrm{A}}\cos\phi_0$ approach $(a\cos\phi_0 / 2)(\partial q_{\mathrm{REF}} / \partial\phi)(\Delta\phi_C)^2$

and $(a\cos\phi_0 / 2)(\partial q_{\mathrm{REF}} / \partial\phi)(\Delta\phi_A)^2$, respectively. At finite amplitude, the role of the QGPV gradient can be different for cyclonic and anticyclonic LWA when q_{REF} has distinct gradients across the reference latitude ϕ_0. In Sections 4 and 6, we will use $\Delta\phi_{\mathrm{C}}$ and $\Delta\phi_{\mathrm{A}}$ to quantify meridional displacements (waviness) of QGPV.

HN16 and HN17 show that A satisfies the canonical conservation relation

$$\frac{\partial\left(A\cos\phi\, e^{-z/H}\right)}{\partial t} + \nabla\cdot\left(\mathbf{F}_{\mathrm{adv}} + \mathbf{F}_{\mathrm{EP}}\right) = n.c., \tag{10}$$

where *n.c.* denotes nonconservative sources and sinks. **F** involves both the zonal advective flux of LWA and three-dimensional radiation stress (Eliassen-Palm flux):

$$\mathbf{F}_{\mathrm{adv}} = e^{-z/H}\left(u_{\mathrm{REF}}A\cos\phi - a\int_0^{\Delta\phi} q_e u_e \cos(\phi+\phi')d\phi', 0, 0\right), \tag{11}$$

$$\mathbf{F}_{\mathrm{EP}} = e^{-z/H}\left(\frac{\cos\phi}{2}\left(v_e^2 - u_e^2 - \frac{R}{H}\frac{e^{-\kappa z/H}\theta_e^2}{\partial\tilde{\theta} / \partial z}\right), -u_e v_e\cos(\phi+\phi'), \frac{f\cos\phi\, v_e\theta_e}{\partial\tilde{\theta} / \partial z}\right), \tag{12}$$

and

$$\nabla\cdot\mathbf{F} \equiv \frac{1}{a\cos\phi}\frac{\partial F_\lambda}{\partial\lambda} + \frac{1}{a\cos\phi}\frac{\partial\left(\cos(\phi+\phi')F_{\phi'}\right)}{\partial\phi'} + \frac{\partial F_z}{\partial z}. \tag{13}$$

In the above R is gas constant, $\kappa = R / c_p$ (c_p is specific heat at constant pressure) and

$$u_e(\lambda,\phi+\phi',z,t) \equiv u(\lambda,\phi+\phi',z,t) - u_{\mathrm{REF}}(\phi,z,t), \tag{14}$$

$$v_e(\lambda,\phi+\phi',z,t) \equiv v(\lambda,\phi+\phi',z,t), \tag{15}$$

$$\theta_e(\lambda,\phi+\phi',z,t) \equiv \theta(\lambda,\phi+\phi',z,t) - \theta_{\mathrm{REF}}(\phi,z,t), \tag{16}$$

where $(u_{\mathrm{REF}}, \theta_{\mathrm{REF}})$ are the reference-state zonal wind and potential temperature inverted from q_{REF} with no-slip bottom boundary condition (HN17, NH18). We treat $(u_{\mathrm{REF}}, \theta_{\mathrm{REF}})$ as time-dependent, since they change with nonconservative processes unlike HN16 wherein the nonconservative effects are ignored. Note also the Taylor identity

$$\nabla\cdot\mathbf{F}_{\mathrm{EP}} = e^{-z/H}\cos\phi\, v_e q_e. \tag{17}$$

The fact that A obeys a relatively simple conservation relation (Equation 10) separates LWA from other metrics of the amplitude of Rossby waves. In the small-amplitude limit after a phase average, $\mathbf{F}_{\mathrm{adv}} + \mathbf{F}_{\mathrm{EP}}$ approaches $(\mathbf{u}_{\mathrm{REF}} + \mathbf{c}_g)A\cos\phi\, e^{-z/H}$, where $\mathbf{c}_g$ is the intrinsic 3D group velocity of the Rossby wave, whereas $\mathbf{u}_{\mathrm{REF}} = (u_{\mathrm{REF}}, 0, 0)$ provides Doppler shifting in the zonal direction. Thus Equation 10 extends previous linear wave activity diagnostics (Plumb, 1985, 1986; Takaya & Nakamura, 2001) and $\rho_0 e^{-z/H} a\cos\phi\, A$ is (minus) the angular pseudomomentum per unit volume of the Rossby waves and geostrophic eddies (ρ_0 is density at $z = 0$).

Following HN17 and NH18, we focus on the density-weighted vertical average, denoted by angle bracket, of Equation 10:

$$\underbrace{\frac{\partial}{\partial t}\langle A\rangle\cos\phi}_{\mathrm{I}} = \underbrace{-\frac{1}{a\cos\phi}\frac{\partial\langle F_\lambda\rangle}{\partial\lambda}}_{\mathrm{II}} \underbrace{-\frac{1}{a\cos\phi}\frac{\partial\langle\cos(\phi+\phi')F_{\phi'}\rangle}{\partial\phi'}}_{\mathrm{III}} \underbrace{+F_z\big|_{z=0}}_{\mathrm{IV}} + \underbrace{\langle\dot{A}\rangle\cos\phi}_{\mathrm{V}}, \tag{18}$$

where

$$F_\lambda = u_{\mathrm{REF}} A\cos\phi + \frac{\cos\phi}{2}\left(v_e^2 - u_e^2 - \frac{R}{H}\frac{e^{-\kappa z/H}\theta_e^2}{\partial\tilde{\theta}/\partial z}\right) - a\int_0^{\Delta\phi} q_e u_e \cos(\phi+\phi')d\phi', \tag{19}$$

$$F_{\phi'} = -u_e v_e \cos(\phi+\phi'), \tag{20}$$

$$F_z\big|_{z=0} = \frac{f\cos\phi}{H}\left(\frac{v_e\theta_e}{\partial\tilde{\theta}/\partial z}\right)_{z=0}. \tag{21}$$

In the above, the terms II and III represent the zonal and meridional convergences of the vertically averaged LWA fluxes, IV is the upward LWA flux at the base, and V is the vertically averaged nonconservative sources and sinks of LWA. Term V will be evaluated as the residual of the budget (Section 5). If one envisions the storm track as a zonal entity in the midlatitudes, term II represents redistribution of LWA within the storm track, whereas terms III - V represent sources-sinks in and out of the track. As shown by HN16, primary contributions to the column LWA come from the upper troposphere, with a secondary contribution from the lower troposphere. Since persistent anomalies of the jet stream tend to be barotropic (e.g., Nakamura & Wallace, 1993), the column LWA is expected to capture the jet-disrupting events in the troposphere reasonably well. For all observational analyses in this paper, we use 1979–2018 ERA-Interim reanalysis (Dee et al., 2011). QGPV and LWA are computed from 6-hourly data with a horizontal resolution of 1.5° × 1.5° interpolated on 49 pressure pseudoheights. Details of the evaluation of the terms in Equation 18 are found in the Supporting Information of HN17 and NH18.

Another important property of LWA is that it covaries negatively with the zonal wind in the storm track regions (HN16, NH18, see also Figure 8 below). A large value of LWA corresponds to a weakened (sometimes even reversed) westerly wind along the latitude circle, and therefore LWA is particularly suited for identifying jet disruptions. In contrast, eddy kinetic energy, which also measures the waviness of the jet stream, tends to maximize where the jet is fastest (HN17). The covariance of LWA and the zonal wind allows us to incorporate wave-flow interaction autonomously into the conservation equation of LWA. This results in a simple nonlinear 1D model similar to that of traffic flow (NH17, NH18, and P19). In Section 5 we will utilize this model to explore the relative roles of eddy forcing and wave-flow interaction in shaping the probability distribution of LWA.

3. Observed LWA and Its Probability Distribution

3.1. Climatology

Figure 2 summarizes seasonal climatology of column LWA $\langle A\rangle\cos\phi$ and its partition into cyclonic and anticyclonic contributions. Values of total LWA show greater zonal and seasonal variations in the Northern Hemisphere (NH) than in the SH. High total LWA over the North Pacific and western Europe in cold seasons marks the enhanced storm track activities, whereas maxima in the southern Eurasia in summer reflect the monsoon circulation. Seasonal-mean values of anticyclonic LWA have notable maxima over the west coast of North America, Western Europe and summer Eurasia, whereas cyclonic LWA dominates in the western end of the Pacific storm track and over the northeast corner of North America in winter. Their distinct patterns reflect the phase structure of the stationary waves: The jet stream (and hence QGPV) is displaced to the north (south) where the anticyclonic (cyclonic) LWA dominates. Total LWA in the SH shows maximum values along the storm track over the Southern Ocean. It is more zonally uniform and less variable than in the NH, but there is a broad maximum in the South Pacific. This maximum is largely associated with anticyclonic LWA, whereas cyclonic LWA is more prevalent in the South Atlantic/Indian Ocean sector of the austral storm track. However, the difference between cyclonic and anticyclonic LWA is generally much weaker than in the NH.

Shown in Figure 3 are the maps of the correlation coefficient r between column LWA and surface temperatures for December/January/February and June/July/August. The correlation is calculated from a linear regression on 40 years of 6-hourly ERA-Interim data (1979–2018), performed after detrending. In both hemispheres, surface temperature generally increases with anticyclonic LWA and decreases with cyclonic LWA,

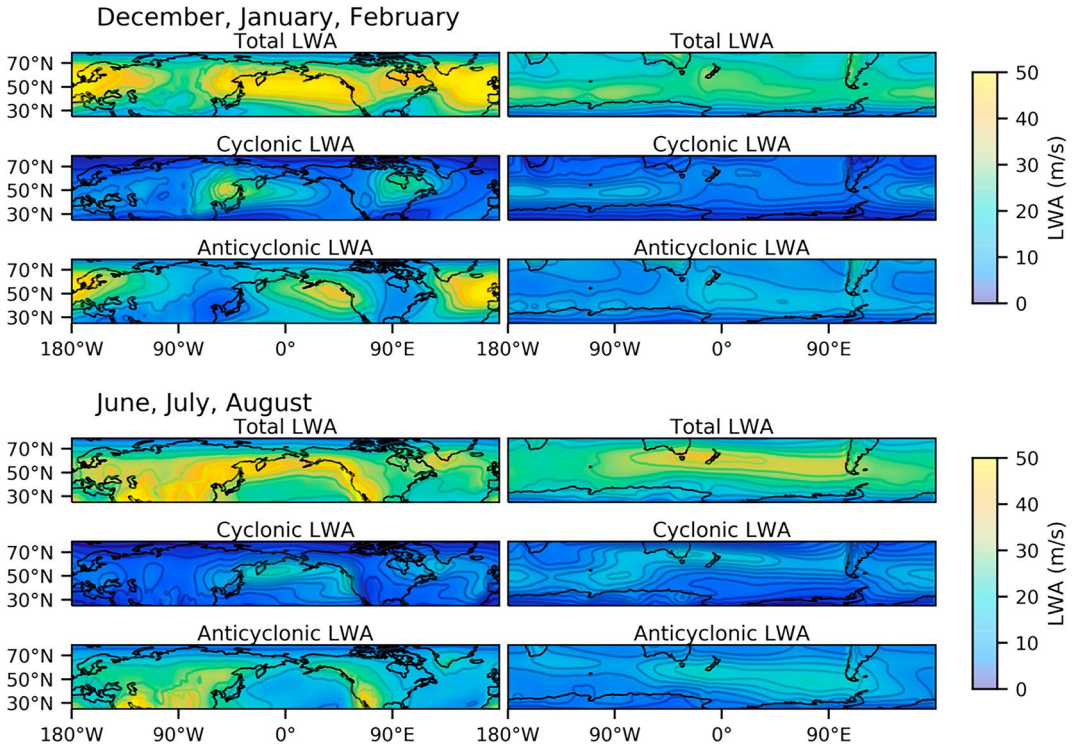

Figure 2. Seasonal climatology of column local wave activity (LWA) $\left(\langle A\rangle\cos\phi, \langle A_C\rangle\cos\phi, \langle A_A\rangle\cos\phi\right)$ between 30° and 80° in latitude for December/January/February (top three rows) and for June/July/August (bottom three). Left column: Northern Hemisphere. Right column: Southern Hemisphere. Based on 40 years of LWA observations [1979–2018, derived from ERA-Interim reanalysis (Dee et al., 2011)].

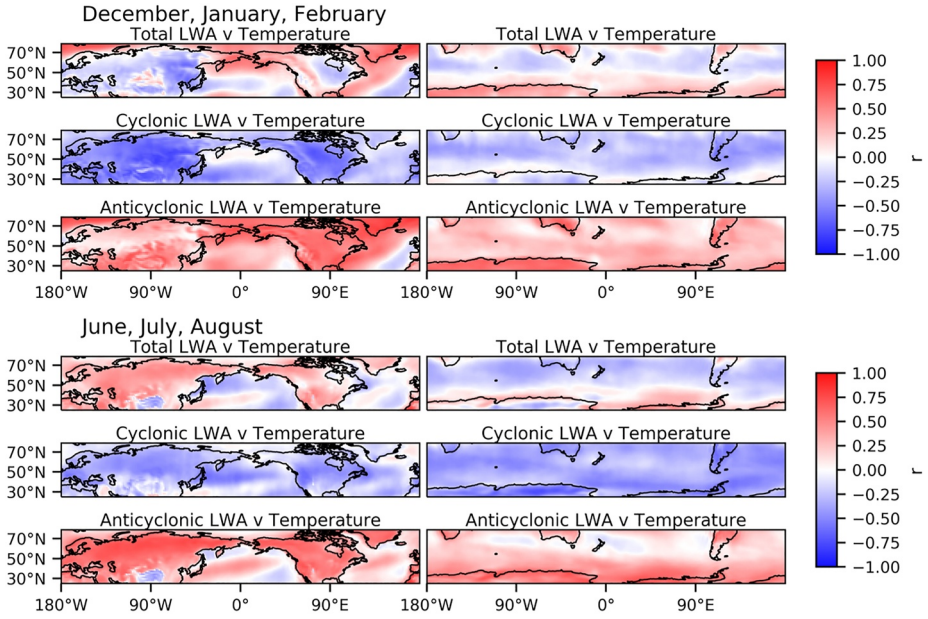

Figure 3. As in Figure 2 but for correlation between components of column local wave activity (LWA) and surface temperatures. Rows 1, 4: Total LWA. Rows 2, 5: cyclonic LWA. Rows 3, 6: anticyclonic LWA. Regression is run on data from 1979 to 2018 derived from the ERA-Interim reanalysis.

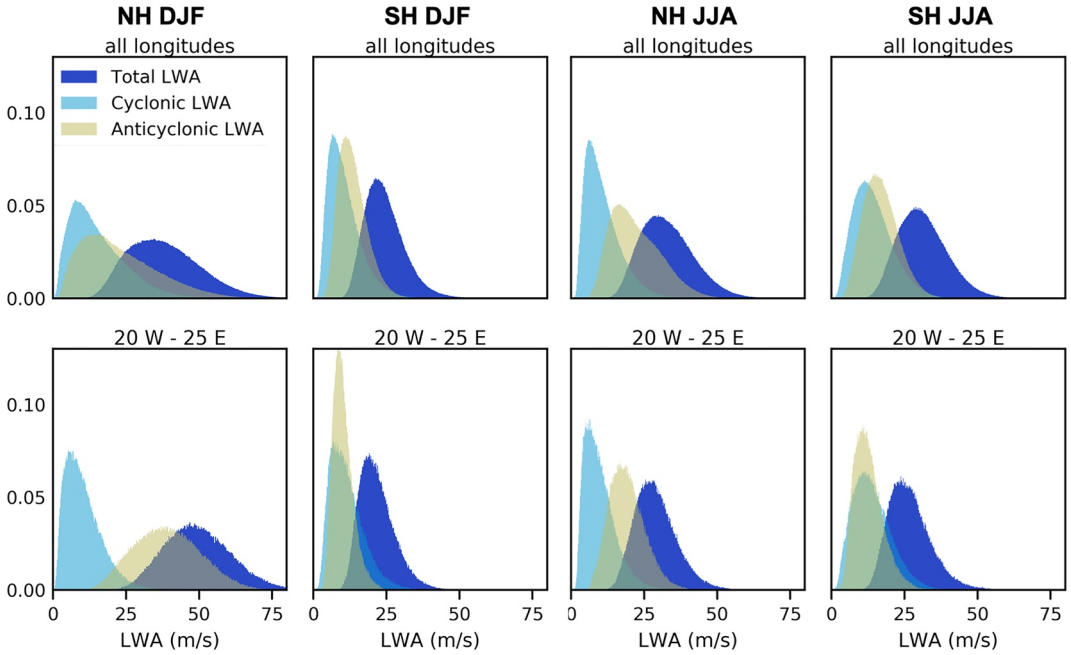

Figure 4. Probability distributions of observed column local wave activity (LWA) from 6-hourly ERA-Interim data (1979–2018). Values of column LWA are averaged over 40° to 50°N (columns 1 and 3) and 40° to 50°S (2 and 4). Top row (a-d): probability distributions over entire zonal circle. Bottom row (e-h): probability distributions for 20°W to 25°E. Left two columns: December/January/February. Right two columns: June/July/August. Each distribution encloses unit area.

and the magnitude of correlation is greater over land surfaces than over the oceans (rows 2, 3, 5, 6). This highlights the dominant role of continents on seasonal timescales. Due to small thermal inertia, the land surfaces are hot in summer and cold in winter, which impacts the stationary wave components of LWA. In the NH, cooling associated with cyclonic LWA dominates in winter so the total LWA correlates negatively with surface temperature over land. In summer, heating with anticyclonic LWA dominates, so the total LWA correlates positively with surface temperature over land. In the SH, the thermal effect of continents on LWA is less clear except over the Antarctica in summer (DJF). Total LWA correlates negatively with surface temperature on the equatorward flank of the storm track and positively on the poleward flank. In winter (JJA), total LWA correlates predominantly negatively with surface temperature in most of the austral storm track.

3.2. Probability Distributions

While seasonal variation of LWA largely reflects changes in the stationary wave amplitude in response to land-sea thermal contrast, blocking and other weather anomalies arise from the internal dynamics of the atmosphere on intraseasonal timescales. To capture the full variability of LWA, it is useful to examine probability distribution constructed from all available data. Figure 4 shows normalized histograms of column LWA (and its partitions) sampled every 6 h from the latitude band of 40° – 50° in both hemispheres for opposite seasons. Generally, the distributions are smooth and unimodal, with an evident positive skew. The skew is even more pronounced in the separate distribution of cyclonic or anticyclonic LWA, and greater in the NH than in the SH. The NH distributions also exhibit greater variance for the same season with both the mode and extreme values shifted to the right compared to the SH, in agreement with Figure 2. In both hemispheres and seasons, the histograms of anticyclonic LWA are slightly shifted to the right relative to those of cyclonic LWA. However, the distribution of anticyclonic LWA varies significantly with longitude and season: For example, the DJF distributions constructed from 20°W-25°E (roughly the longitudes of western Europe) show a much higher median value for anticyclonic LWA in the NH (Figure 4e) and a much higher peak in the SH (Figure 4f) compared to the distributions sampled from all longitudes. During JJA, the NH

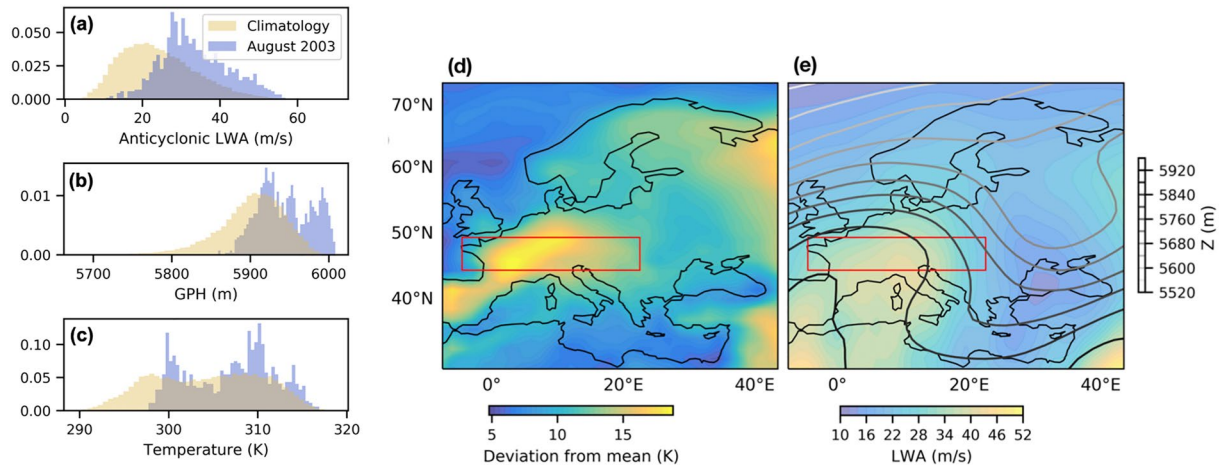

Figure 5. European heat wave of August 2003 in different metrics. (a) Probability distribution of August anticyclonic local wave activity (LWA) over Europe. The sampling region (45° to 50°N and 4.5°W to 22.5°E is marked by a red box in (d) and (e). Based on 6-hourly ERA-Interim reanalysis. Beige: climatology. Blue: August 2003. (b) Same as (a) but for 500 hPa geopotential height. (c) Same as (a) but for surface temperature. (d) Surface temperature anomaly averaged over August 2–13, 2003. (e) Geopotential height (contours) and anticyclonic column LWA (color) averaged over August 2–13, 2003.

anticyclonic LWA in the same region has a significantly narrower distribution than the global distribution (Figures 4g and 4c).

Often high values of LWA coincide with periods in which the jet stream is disrupted, and as such, during an extreme weather event associated with a stalled jet one can expect anomalously high LWA (HN16, NH18). In Figure 5 we plot one such event: The European heat wave of August 2003, which caused tens of thousands of deaths and was at least partially due to strong anticyclonic blocking (Garcia-Herrera et al., 2010). During this period, values of anticyclonic LWA, geopotential height, and surface temperature all deviated positively from the seasonal mean over Europe, indicating the connection between anomalous values of LWA and extreme weather (Figures 5a–5c). At the height of the heat wave (August 2–13), surface temperatures in central Europe were nearly 20 K above average (Figure 5d) and they were accompanied by an enhanced quasi-stationary ridge in geopotential height and very large anticyclonic LWA (Figure 5e). The jet stream is seen diverted to the north and the normal eastward weather migration was disrupted.

4. Anatomy of Probability Distribution

In Section 2 we rendered LWA as a function of gradient and displacement of q_{REF} (Equations 8 and 9). Here we dissect the relationship between the probability distributions of LWA and those of displacement at 45°N (two left columns of Figure 6) and at 45°S (right column) for winter months. These latitudes are, on average, inside the storm track(s) of each hemisphere during winter (Shaw et al., 2016). To extract persistent signals, we average all quantities over 4 days in this section. The top row of Figure 6 plots cyclonic and anticyclonic LWA $\left(\langle A_{\mathrm{C}}\rangle\cos 45°\text{ and }\langle A_{\mathrm{A}}\rangle\cos 45°\right)$ against column equatorward and poleward displacements $\left(\langle\Delta\phi_{\mathrm{C}}\rangle\text{ and }\langle\Delta\phi_{\mathrm{A}}\rangle\right)$, respectively (here the sign of $\Delta\phi_{\mathrm{C}}$ is reversed for an easy comparison). As suggested by Equations 8 and 9, the two variables form a compact relationship, readily approximated by a polynomial fit. Curvature of the fitted curve corresponds to the gradient of q_{REF}. The curves are symmetric, suggesting that asymmetry in the gradient of q_{REF} across these latitudes is insignificant. However, the shape of the curve is different between 45°N and 45°S, reflecting the different profiles of q_{REF} in the two hemispheres. While the relationship between the displacement and LWA is robust in each hemisphere, probability distribution of displacement varies significantly from one location to another (Figures 6d–6f). At 45°N, both poleward and equatorward displacements are broadly distributed about the mode, with the poleward displacement appreciably greater (the mode being 10° versus 6.5°, Figure 6d). Therefore, anticyclonic LWA would involve deeper intrusion from the south than cyclonic LWA would do from the north. The asymmetry grows when the histogram is constructed for 20°W-25°E: While the mode for the equatorward displacement remains unchanged, the mode for the poleward displacement increases to about 12.5° with distinctly narrower

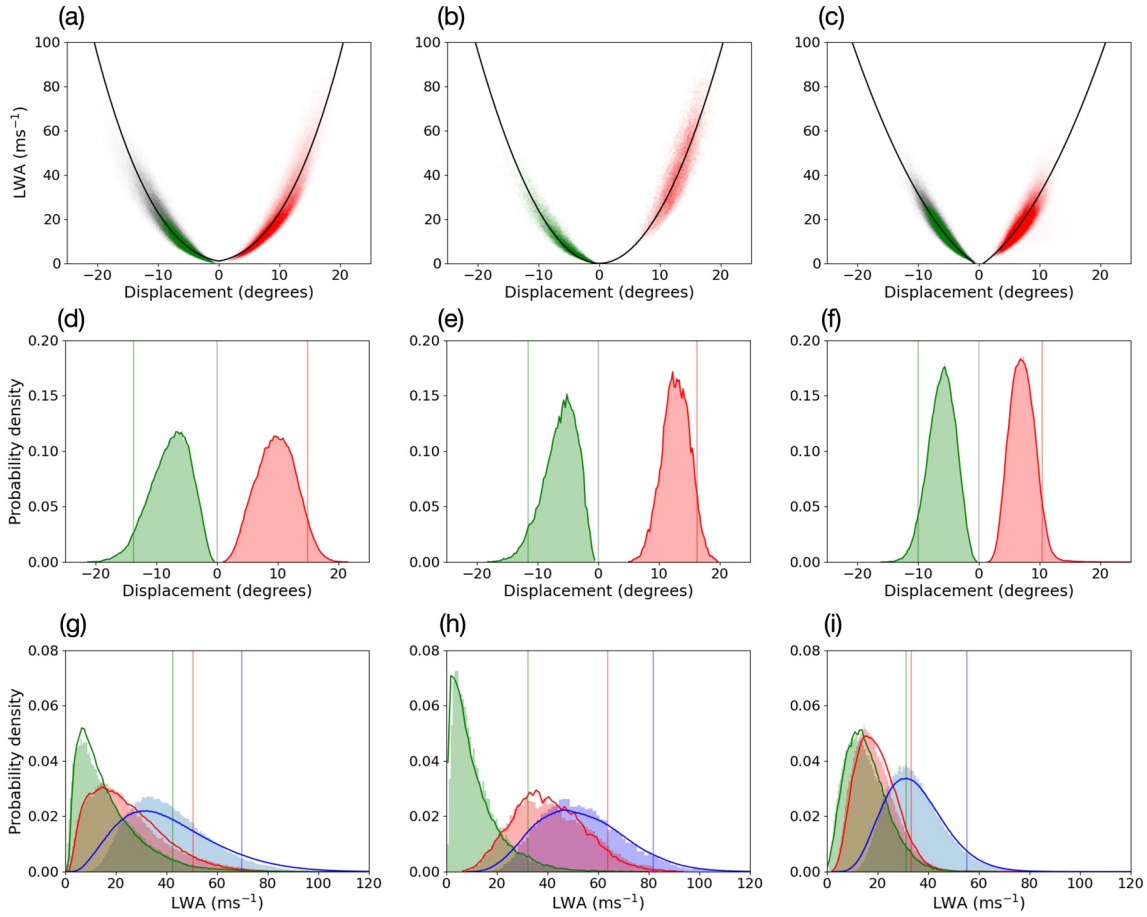

Figure 6. Properties of the observed local wave activity (LWA) distributions at 45°N during December/January/February (DJF) (left two columns) and at 45°S during June/July/August (JJA) (right column). The left and right columns are based on the data sampled from all longitudes, whereas the middle column samples only from 20°W-25°E at 45°N. Top row (a–c): relationship between the column-mean displacement and the column-mean LWA. Red: anticyclonic LWA. Green: cyclonic LWA. Positive (poleward) displacements are $\Delta\phi_A$, whereas negative (equatorward) displacements are $-\Delta\phi_C$ in degrees. Solid curves are polynomial fit to the relations. Middle row (d–f): probability distributions of column-mean displacement. Red: poleward displacement associated with anticyclonic LWA. Green: equatorward displacement associated with cyclonic LWA. Vertical lines indicate the 95 percentile mark in each distribution. Bottom row (g–i): probability distributions of LWA. Blue shade: total LWA. Green shade: cyclonic LWA. Red shade: anticyclonic LWA. Vertical lines are the 95 percentile marks. Red and green curves are based on the displacement distributions in (d–f), rescaled using the fitted relationships between the displacement and LWA in (a–c). The blue curve is the joint probability distribution of cyclonic and anticyclonic LWA, assuming that they are mutually independent. Based on 1979–2018 ERA-Interim reanalysis. The 6-hourly data are time averaged over nonoverlapping 4-day periods before the analysis.

distribution (Figure 6e). This reflects a quasi-stationary ridge that develops over Europe in winter (Woollings et al., 2018), which pushes the QGPV contours preferentially toward the pole. At 45°S, the distributions of cyclonic and anticyclonic displacements are more symmetric and they are both narrower. The modes are also smaller than in the NH, that is, the QGPV is generally much less wavy in the austral winter than in the north (Figure 6f).

The probability distributions of displacement and those of LWA are related through the one-to-one relationship between the two variables (Figures 6a–6c). In Figures 6g–6i, the red and green curves for the LWA distributions are computed from the corresponding distributions of displacement in Figures 6d–6f and rescaling the variables using the fitted relationships in Figures 6a–6c. They reproduce the observed distributions of cyclonic and anticyclonic LWA (shading) reasonably well. The distributions of cyclonic and anticyclonic LWA are more skewed than the corresponding distributions of displacements because LWA increases with increasing displacement, giving more weight on the large values in the distribution. At 45°N, anticyclonic LWA has a markedly broader distribution and a greater mode than cyclonic LWA because of the greater displacement (Figures 6g, 6h and 6d, 6e). The blue curves in Figures 6g–6i are estimated as joint

probability distributions of cyclonic and anticyclonic LWA, assuming that the two are mutually independent. They capture the shapes of the observed total LWA distributions qualitatively (blue shade). In reality, there is a weak but nonnegligible negative correlation between cyclonic and anticyclonic LWA (for example, $r = -0.36$ for Figure 6g) and this leads to an appreciable mismatch between the joint distribution and the observed distribution.

While the above analysis elucidates the relationship between the distributions of displacement and those of LWA and why the latter are more skewed, this alone does not explain the shape of the LWA distributions (insofar as we do not have a theory for the observed distributions for displacement). In the next section, we use a simple 1D model to address the dynamical controls of the LWA distribution more directly.

5. LWA Distributions in a One-Dimensional Model

5.1. Column Budget of LWA

To formulate the 1D model of LWA, we first evaluate the terms in the column budget of LWA (Equation 18) with reanalysis data. Since large-amplitude wave events typically evolve on the timescales of a few days to a week, we evaluate the LWA budget over 4-day periods. The averaging largely filters out variations associated with phase propagation of the waves. Following NH18, we split the entire observational period into nonoverlapping 4-day periods. We then integrate all terms in Equation 18 over the 4 days of each period. This yields $(A(t) - A(t-4\,\text{days}))\cos\phi \equiv \Delta_A$ on the L.H.S. and the average of 16 consecutive 6-hourly data for each term on the R.H.S. We then multiply all terms by Δ_A and take the average over all 4-day periods (an ensemble of 858 for DJF and 880 for JJA):

$$\underbrace{\overline{\overline{(\Delta_A)^2}}}_{\text{(i)}} = \underbrace{\overline{\overline{\Delta_A \cdot \int(\text{II})dt}}}_{\text{(ii)}} + \underbrace{\overline{\overline{\Delta_A \cdot \int(\text{III})dt}}}_{\text{(iii)}} + \underbrace{\overline{\overline{\Delta_A \cdot \int(\text{IV})dt}}}_{\text{(iv)}} + \underbrace{\overline{\overline{\Delta_A \cdot \int(\text{V})dt}}}_{\text{(v)}}, \tag{22}$$

where double bars indicate ensemble mean. This is an equation for 4-day variance of LWA, and the R.H.S. terms quantify their contributions to the variance.

Figure 7 shows all these terms averaged over 30°-60°N and 30°-60°S for opposite seasons. In the NH winter (Figure 7a), the 4-day variance of LWA [term (i)] is elevated over 130-240°E and 50°W-30°E, which mark the Pacific and Atlantic storm tracks. Except at a few locations, nearly all of the variance is explained by term (ii), namely, the zonal convergence of wave activity flux. Interestingly, terms (iii) and (iv), which are the main drivers of wave activity in the zonal-mean formalism (Edmon et al., 1980), correlate negatively with Δ_A, particularly in the Pacific storm track (Figure 7a, blue curve). These terms inject wave activity as wave packets exit the region eastward, leading to the negative correlation locally, but they amplify the wave packet following its eastward movement, consistent with the notion of downstream development (Chang, 1993; Wirth et al., 2018). The residual term (v) becomes comparable to term (ii) in the eastern Pacific and over North America, which may reflect latent heating (diabatic source) as well as a sink due to mixing associated with wave breaking (Nakamura & Zhu, 2010).

Term (ii) plays an even more dominant role in the austral winter (Figure 7b), where contributions from terms (iii)-(v) are altogether secondary. Apart from some elevation in the Indian Ocean sector (80-150°E) and a spike due to interference with the Andes $(\sim 290°\text{E})$, the variance of LWA is more zonally uniform than in the NH. During the boreal summer, the LWA variance is overall about one half of that in winter, and term (ii) explains about 70 percent of it, significantly less than in winter but it is still the leading term, while term (v) takes up the remaining 30 percent (Figure 7c). A likely cause of the enhanced residual is heating of land surfaces and latent heat of condensation associated with summer monsoons. As in the NH, the LWA variance in the austral summer is much lower than its winter counterpart (Figure 7d). Yet unlike the boreal summer, term (ii) continues to explain virtually all of the variance, except 100-130°E where term (v) shows an elevated influence, an indication of less pronounced role of summer monsoons in the SH. Overall the analysis demonstrates the predominant role of the convergence of the zonal flux of LWA on synoptic timescales, that is, the predominant balance of terms in Equation 18 is between I and II (We have also tested the budget for 8-day variance and found the results essentially similar.) Therefore, the nature of the zonal LWA flux $\langle F_\lambda \rangle$ should be a key determinant of the variability of LWA on these timescales.

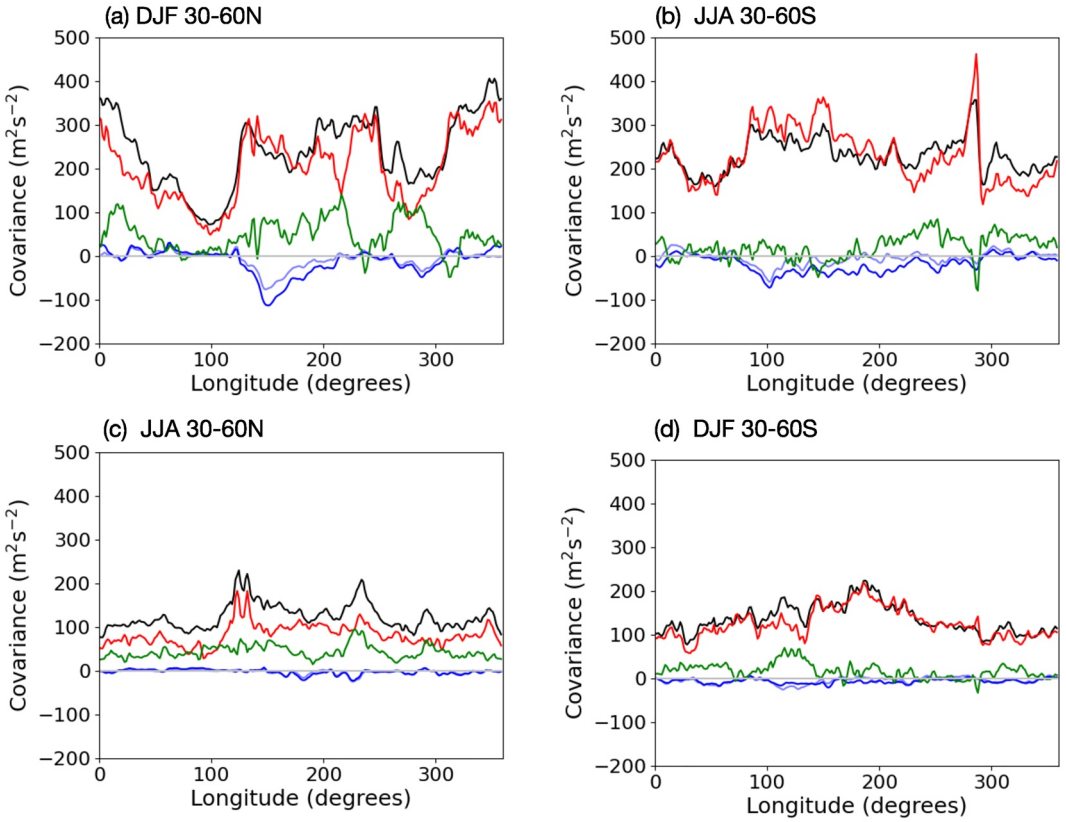

Figure 7. Longitudinal distributions of the terms in Equation 22. (a) Average of 30°-60°N during December/January/February (DJF). Black: term (i). Red: term (ii). Blue: terms (iii)+(iv). Thin blue: term (iv). Green: term (v). (b) Same as (a) but the average of 30°-60°S during June/July/August (JJA). (c) Same as (b) but the average of 30°-60°N during JJA. (d) Same as (c) but the average of 30°-60°S during DJF. See text for details.

5.2. The 1D Model

HN16 and NH18 demonstrate the tendency that the column LWA covaries negatively with the column zonal wind in the storm tracks of the NH winter. This means that where the jet stream meanders more, the eastward wind along the latitude circle diminishes and vice versa, a clear evidence of (nonlocal) wave-flow interaction. Figure 8 extends their analysis to all longitudes at 45°N and 45°S for winter and summer months, showing the slope (red) and intercept (blue) of local linear regression between column LWA $\langle A\rangle\cos\phi$ and column zonal wind $\langle u\rangle\cos\phi$. Overall, despite significant scatter ($r^2 \sim 0.4-0.5$), their negative correlation is robust in both hemispheres throughout the year with the magnitude of slope 0.3–0.4, and the intercept values for $\langle u\rangle\cos\phi$ are also fairly uniform zonally. This justifies a first approximation

$$\langle u\rangle \approx u_0 - \alpha\langle A\rangle, \quad \alpha > 0, \tag{23}$$

where α is the magnitude of the regression slope of $\langle u\rangle$ and $\langle A\rangle$ and measures the strength of eddy-zonal flow interaction, whereas u_0 is a constant wind speed. Using Equation 23, NH18 simplify Equation 18 into a 1D equation for the column LWA

$$\frac{\partial}{\partial t}\langle A\rangle = -\frac{\partial}{\partial x}\left[\left(u_0 + c_g - \alpha\langle A\rangle\right)\langle A\rangle\right] + S - \frac{\langle A\rangle}{\tau} + \kappa\frac{\partial^2\langle A\rangle}{\partial x^2}, \tag{24}$$

where the first term on the R.H.S. replaces term II in Equation 18. The three components of the zonal flux of LWA correspond to the three terms in Equation 19: u_0 replaces u_{REF}, c_g is the intrinsic zonal group velocity, and $-\alpha\langle A\rangle$ in Equation 23 replaces u_e under the barotropic assumption. The other terms are represented by a source term S plus linear damping and diffusion of $\langle A\rangle$. By further partitioning $\langle A\rangle$ into the base-level

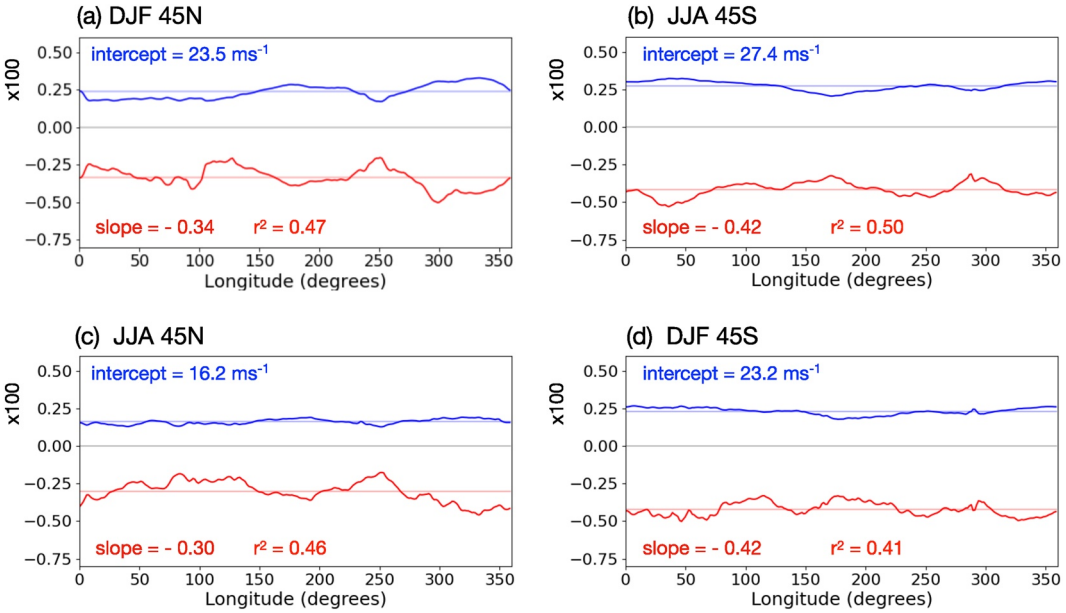

Figure 8. Red: Longitudinal distributions of the slope of linear regression between column local wave activity (LWA) $\langle A\rangle\cos\phi$ and column zonal wind $\langle u\rangle\cos\phi$ at $\phi = 45°$ N and 45°S. Blue: corresponding intercept values for $\langle u\rangle\cos\phi$ divided by 100 at $\langle A\rangle\cos\phi = 0$. Regression is based on 858 (December/January/February [DJF]) and 880 (June/July/August[JJA]) 4-day averaged values of $\langle A\rangle\cos\phi$ and $\langle u\rangle\cos\phi$ at each longitude. (a) DJF at 45°N. (b) JJA at 45°S. (c) JJA at 45°N. (d) DJF at 45°S. The zonal-mean values of the intercept, slope and r^2 are noted in each panel. The intercept and slope corresponds to u_0 (times $\cos\phi$) and $-\alpha$, respectively, in Equation 23. Based on 1979–2018 ERA-Interim.

(steady, stationary wave component) $A_S(x)$ and the transient component $\hat{A}(x,t)$, NH18 derive the equation for $\hat{A}$ as

$$\frac{\partial}{\partial t}\hat{A} = -\frac{\partial}{\partial x}\left[\left(C(x) - \alpha\hat{A}\right)\hat{A}\right] + \hat{S} - \frac{\hat{A}}{\tau} + \kappa\frac{\partial^2\hat{A}}{\partial x^2}, \quad C(x) \equiv u_0 + c_g - 2\alpha A_S(x). \tag{25}$$

Equation 25 is analogous to the equation that describes traffic flow on a highway (NH18). Spontaneous disruption of the westerly wind occurs just like traffic congestion, when $\hat{A}$ grows past the value that maximizes the nonlinear zonal flux of LWA $(C(x) - \alpha\hat{A})\hat{A}$. This maximization occurs at

$$\hat{A} = \frac{C(x)}{2\alpha} \tag{26}$$

or equivalently at

$$\langle A\rangle = \hat{A} + A_S(x) = \frac{u_0 + c_g}{2\alpha}. \tag{27}$$

Although the R.H.S. of Equation 27 is independent of x, the disruption is more likely to occur where $A_S(x)$ is large [viz. $C(x)$ is small] and the required $\hat{A}$ for Equation 26 is smaller; therefore the stationary wave localizes the preferred region of block formation. The structure of $A_S(x)$ may be inferred from the minimum observed value of LWA for each season, which is shown in red curves in Figure 9. The seasonal minimum LWA comprises approximately one half of the seasonal mean LWA (Figure 2), and the two show similar structures. In the NH, they both vary significantly in longitude, with distinctive maxima in the downwind regions of the Pacific and Atlantic storm tracks in winter and over East Asia and the Rockies in summer. In the SH their longitudinal variation is more modest with a broad maximum around 170°E. Also plotted in Figure 9 is the seasonal-mean zonal wind $\langle\overline{u}\rangle$ (blue curves). It is generally weaker (stronger) where the LWA is greater (smaller), consistent with Equation 23.

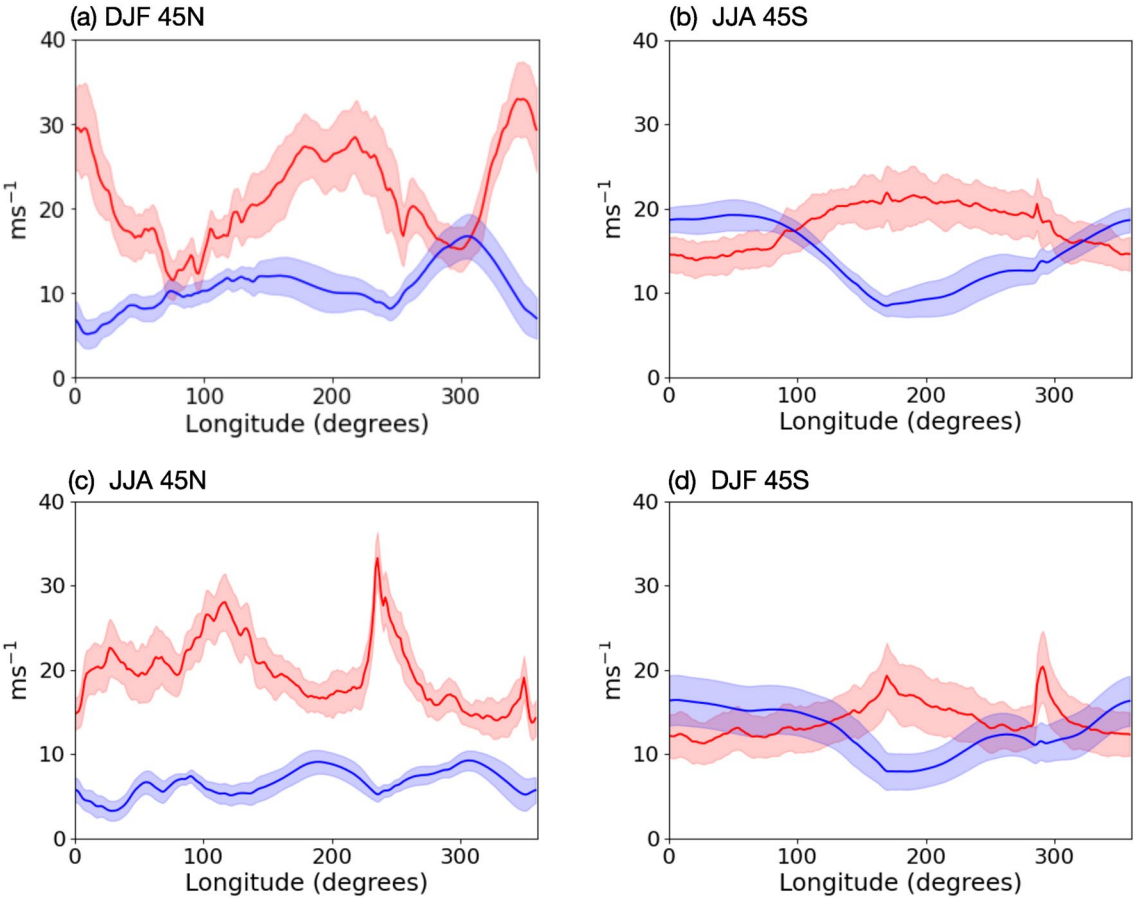

Figure 9. Seasonal minimum column local wave activity (LWA) $\langle A \rangle_{\min} \cos\phi$ (red) and the seasonal-mean column zonal wind $\langle \overline{u} \rangle$ (blue) as functions of longitude at $\phi = 45°$N and 45°S. Shading indicates ± one standard deviation associated with interannual variability. Based on ERA-Interim reanalysis (1979–2018).

Equation 25 has been shown to reproduce salient features of Atlantic blocks in the NH winter (NH18). Subsequently P19 examined blocking statistics with Equation 25 using pseudostochastic eddy forcing $\hat{S}$, varying parameters of the flow. They found that a reduced jet speed u_0 and/or an enhanced stationary wave amplitude in A_S are conducive to block formation, as is stronger eddy forcing $\hat{S}$. Here we follow P19 and use Equation 25 to examine the probability distribution of LWA produced by the model. The model setup is similar to P19 except for the transient and stationary eddy forcing. Instead of the synthetic transient eddy forcing used by P19, we use observed spectra of eddy forcing for prescribing $\hat{S}$. Figure 10a shows spectral amplitudes of the sum III + IV + V (= I–II) in Equation 18 for SH summer (DJF) averaged over 40-60°S. The eddy forcing is strongest in the intra-seasonal to synoptic timescales for zonal wavenumbers 4–6 and shows a clear tendency of eastward propagation, consistent with Wang and Nakamura (2016). Figure 10b shows the histogram of the sum of these terms sampled from all longitudes, based on the 6-hourly ERA-Interim reanalysis. The transient eddy forcing distribution is symmetric between positive and negative values. We then approximate this forcing by a superposition of 2,400 waves with 20 zonal wavenumbers and 120 frequency bands between ±0.6 cycles per day (CPD), whose amplitudes are given by Figure 10a. The phase of each wave component is randomized initially and subsequently translated according to its phase velocity. The distribution of this spectrally reconstructed forcing, after multiplying by a constant to match the observed variance in Figure 10b is shown in Figure 10c. Compared to Figure 10b, some extreme values are lost due to truncation of high frequencies, but overall the symmetric shape of the distribution is preserved. We call this forcing $\hat{S}_0(x,t)$ and use it for all subsequent experiments with varying magnitude ε and a constant offset S_{00}:

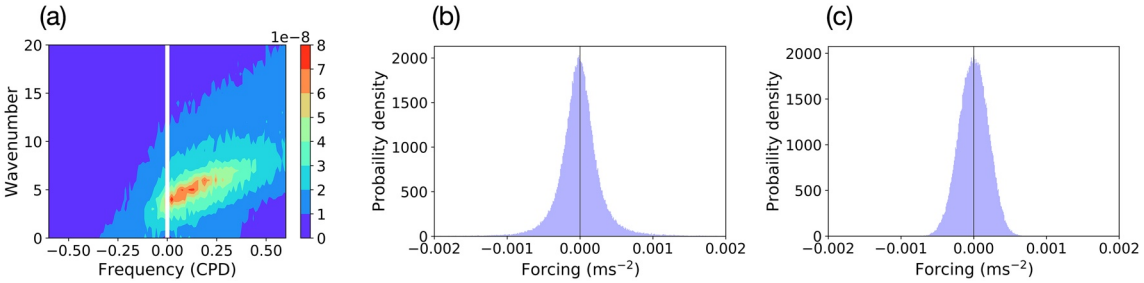

Figure 10. (a) Spectral amplitude of transient eddy forcing [terms III + IV + V = I–II in Equation 18] for December/January/February (DJF) averaged over 40°-60°S as a function of frequency and zonal wavenumber. Positive (negative) frequencies correspond to eastward (westward) propagation. (b) Distribution of the transient eddy forcing for the same period and region. Both (a) and (b) are based on 6-hourly ERA-Interim data for 1979–2018. (c) Distribution of transient forcing spectrally reconstructed with 20 zonal wavenumbers and frequencies between ±0.6 cycle per day (CPD).

$$\hat{S}(x,t) = \varepsilon \hat{S}_0(x,t) + S_{00}. \tag{28}$$

The positive offset S_{00} is introduced to maintain a positive global mean LWA, A_{00}, since the global mean of $\hat{S}_0$ is zero. A_{00} and S_{00} are related through the global mean of Equation 25

$$S_{00} - A_{00} \,/\, \tau = 0. \tag{29}$$

S_{00} may be thought of as the aggregate sources of LWA (e.g., low-level poleward heat flux and latent heat).

For the experiments with a stationary wave, we impose a wavenumber 2 stationary wave, consistent with Figure 9a, which modulates C according to Equation 25:

$$A_S(x) = \Gamma \cos(4\pi x \,/\, L), \qquad C(x) = U_j - 2\alpha\Gamma \cos(4\pi x \,/\, L), \tag{30}$$

where $L = 28000$ km is the channel length and Γ is the amplitude of the stationary wave.

In the following, we vary four parameters of the model one at a time: the strength of nonlinearity α, the amplitude of transient eddy forcing ε, the amplitude of the stationary wave Γ, and the Doppler-shifted group velocity of Rossby waves in the wave-free reference state, $U_j \equiv u_0 + c_g$. For the transient Rossby waves in the troposphere, U_j is dominated by the advection by the zonal wind u_0 [e.g., Plumb (1986), p.1668]. Therefore the variation of U_j may be thought of as the variation of the flow speed u_0, and for this reason (and following P19) we call U_j as "jet speed" hereafter. For the first three sets of experiments we do not impose stationary wave forcing $(\Gamma = 0)$ and ignore damping in Equation 25 $(\tau = \infty)$. We then initialize $\hat{A}$ with a constant A_{00}, which defines the mean value of LWA, while letting $S_{00} = 0$, consistent with Equation 29. Since our main focus here is the shape of the probability distribution and not the determinism of its mean value (we will address this in Section 6.2), we treat A_{00} as an external parameter and choose $A_{00} = 26$ ms^{-1}. The following results are qualitatively similar for a range of A_{00} as long as $U_j - 2\alpha A_{00} > 0$ [see Equation 34 below]. We drive the model with the above eddy forcing Equation 28 with $S_{00} = 0$ for 933 days and repeat the experiment six times, each time randomizing the phase in the transient eddy forcing. (It typically takes only 3–4 iterations for the probability distribution to converge. See Appendix for numerical details of the model.) For the experiments with a stationary wave, we first integrate Equation 25 from $\hat{A} = 0$ with $S_{00} = 3 \times 10^{-5}$ ms^{-2} and $\tau = 10$ days but without transient eddy forcing ($\varepsilon = 0$) for 100 days to obtain a steady state with a mean value of 26 ms^{-1} plus a stationary wave structure. Once the steady state is reached, we turn on the transient eddy forcing and continue to run the model for additional 933 days, during which the output is collected every 6 h. We then repeat the experiment six times, each time randomizing the phase of the transient eddy forcing.

5.3. Modeled LWA Distributions

Figure 11 displays the probability distributions of 4-day averaged LWA predicted by the model. LWA is measured relative to the mean value $\left(A_{00} = 26\text{ms}^{-1}\right)$ and normalized by $U_j - 2\alpha A_{00}$ (See Section 5.4 for the

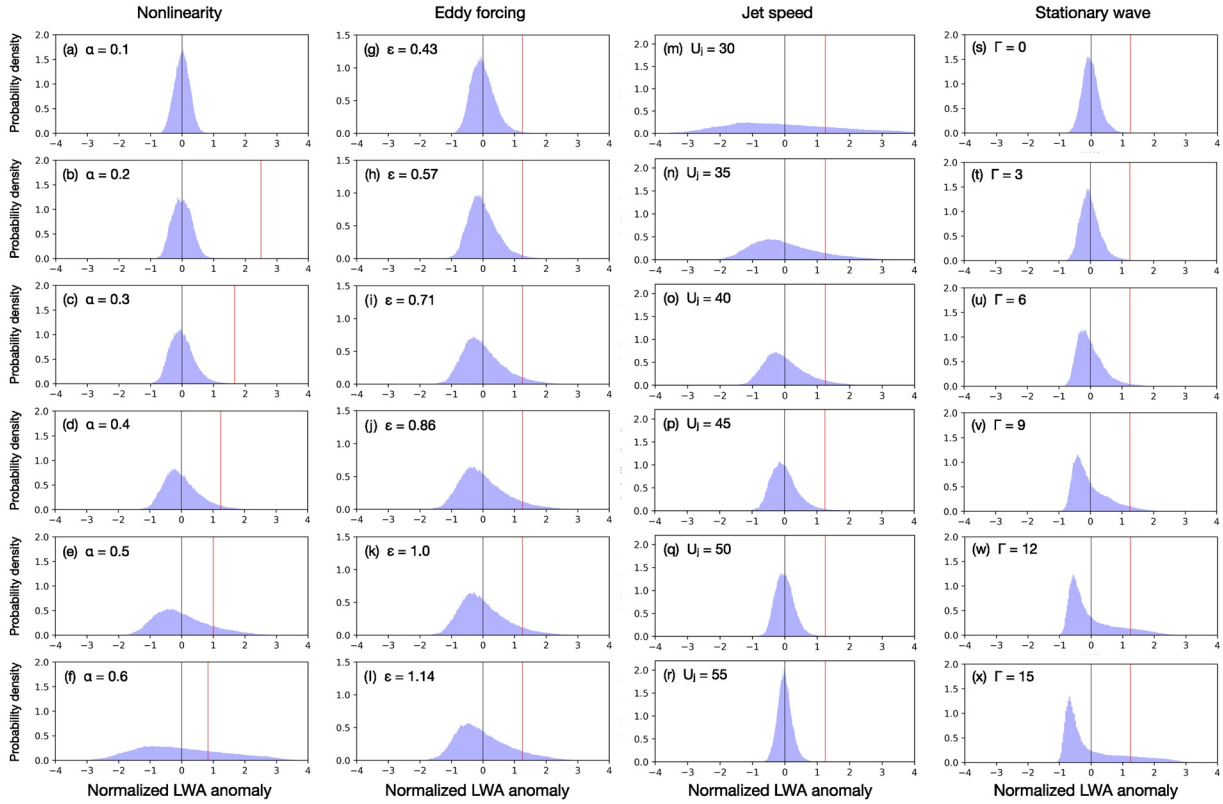

Figure 11. Probability distributions of 4-day averaged local wave activity (LWA) relative to its mean value in the 1D model, as functions of various parameters. LWA is normalized by $U_j - 2\alpha A_{00}$, where A_{00} is the mean value of LWA, which is 26 ms^{-1} in all cases. Column 1 (a–f): α (nonlinearity) is increased from 0.1 (a) to 0.6 (f). $U_j = u_0 + c_g = 40$ ms^{-1}, $\varepsilon = 0.71$, $\Gamma = 0$. Column 2 (g–l): transient forcing amplitude (ε) is increased from 0.43 (g) to 1.14 (l). $\alpha = 0.4$, $U_j = 40$ ms^{-1}, $\Gamma = 0$. Column 3 (m–r): jet speed U_j is varied from 30 (m) to 55 ms^{-1} (r). $\alpha = 0.4$, $\varepsilon = 0.86$, $\Gamma = 0$. Column 4 (s–x): stationary wave amplitude (Γ) is increased from 0 (s) to 15 ms^{-1}(x). $\alpha = 0.4$, $\varepsilon = 0.43$, $U_j = 40$ ms^{-1}. The red vertical lines (= $0.5\alpha^{-1}$) indicate the spontaneous blocking threshold. See text for details.

rationale for nondimensionalization.). In the first column of Figure 11, we fix transient eddy forcing and jet speed and vary the strength of nonlinearity α. When α is small, LWA has a narrow, symmetric distribution about the mean value (Figures 11a and 11b). As α increases, the distribution spreads and develops positive skew similar to observation (Figures 11c–11e). Since the distribution of forcing is symmetric (Figure 10c), skewness clearly arises from the nonlinearity in the zonal advection of LWA. As α increases, the threshold for spontaneous jet disruption [Equation 27; in nondimensional form $0.5\alpha^{-1}$] decreases, as indicated by the red line. By $\alpha \sim 0.5 - 0.6$, a significant portion of the distribution lies above the threshold, increasing the probability of jet disruption (Figures 11e and 11f).

In the second column of Figure 11, we vary the strength of transient eddy forcing ε with $U_j = 40$ ms^{-1} and $\alpha = 0.4$. Increasing ε does not change the skewness or the threshold value, but it does make the distribution more spread. As a result, more fraction of the distribution exceeds the threshold at higher transient eddy forcing (Figures 11g-11l). The jet speed U_j also affects the distribution greatly. As seen in the third column, a weak jet makes the LWA distribution very broad for a fixed transient eddy forcing and α (Figures 11m, 11n). The distribution narrows as the jet speed increases, and since the jet speed does not affect the non-dimensional threshold, probability of LWA above the threshold diminishes. Naturally, this means that it is harder to disrupt a faster jet.

The last column of Figure 11 depicts the effects of the stationary wave amplitude Γ. The behavior of the distribution is similar to the case with varying transient eddy forcing at small amplitude: The distribution spreads with an increasing Γ (Figures 11s–11u). At large amplitude, however, the distribution evolves into a distinct shape: While a tall peak remains at low (below average) values, there also develops a long tail at

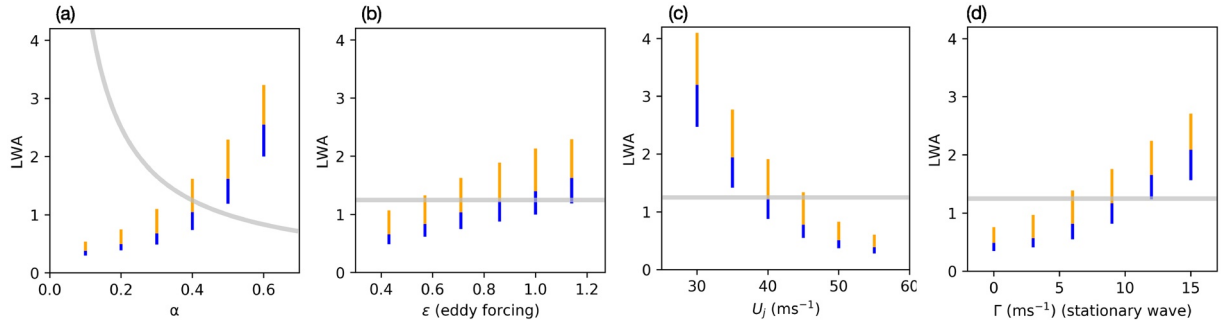

Figure 12. Extreme values of nondimensional local wave activity (LWA) in the four columns of Figure 11. The gray curves indicate the threshold values. The blue and orange lines denote ensemble-mean 90th–95th and 95th–99th percentile values, respectively. The LWA values are plotted against (a) α (nonlinearity); (b) ε (transient eddy forcing); (c) U_j (jet speed); and (d) Γ (stationary wave amplitude). See caption of Figure 11 for other parameters used.

high values of LWA (Figures 11w, 11x). This dichotomy reflects high values of LWA (i.e., a highly meandering jet) occasionally forming around the stationary ridges of LWA while low values filling everywhere else. A significant portion of the former exceeds the threshold.

5.4. Sensitivity of LWA Extremes to Parameters

Figure 12 summarizes the sensitivity of LWA extremes to the four parameters of the model, as well as the nondimensional threshold for jet disruption ($= 0.5\alpha^{-1}$) computed for each parameter combination. Extreme values of LWA increase with increasing α, while the threshold value decreases as α^{-1}. As a result (for $U_j = 40$ ms^{-1} and $\varepsilon = 0.71$), the 95th–99th percentile values of LWA begin to cross the threshold at $\alpha = 0.4$ and by $\alpha = 0.5$ all 90th–99th percentile values are above the threshold (Figure 12a). As the LWA distribution spreads with an increasing α, the ranges of 90th–95th and 95th–99th percentile values also increase. Crossing of the threshold is more gradual with the increasing magnitude of transient eddy forcing (ε), but probability of LWA exceeding the threshold increases with ε nonetheless (Figure 12b). Meanwhile, LWA decreases as the jet speed U_j increases (Figure 12c). For $\alpha = 0.4$ and $\varepsilon = 0.86$, the extreme values are mostly below threshold for $U_j > 45$ ms^{-1}, so there will be few to no jet disruption events. Increasing stationary wave amplitude also increases the probability of extreme events exceeding the threshold, slightly faster than the transient eddy forcing (Figure 12d). Overall, these observations are consistent with the findings of P19 despite the different forcing formulations, attesting to the robustness of the results.

Although the model solves for LWA in a dimensional form, it is useful to nondimensionalize the governing equation to shed light on the results. For example, in the absence of stationary wave $[A_0(x) = 0, C(x) = U_j]$ and damping, Equation 25 becomes (see Appendix)

$$\frac{\partial}{\partial t}\hat{A} = -\frac{\partial}{\partial x}\left[\left(U_j - \alpha\hat{A}\right)\hat{A}\right] + \hat{S} + \kappa\frac{\partial^2\hat{A}}{\partial x^2}, \qquad \kappa = 0.1\frac{(\Delta x)^2}{\Delta t}, \qquad \hat{S} = \varepsilon\hat{S}_0(x,t). \tag{31}$$

With the scaling

$$x \equiv Lx^{\dagger}, \qquad t \equiv \frac{L}{U_j - 2\alpha A_{00}}t^{\dagger}, \qquad \hat{A} \equiv A_{00} + \left(U_j - 2\alpha A_{00}\right)A^{\dagger} \tag{32}$$

and

$$\Delta x \equiv L\Delta x^{\dagger}, \qquad \Delta t \equiv \frac{L}{U_j - 2\alpha A_{00}}\Delta t^{\dagger}, \tag{33}$$

where the quantities with dagger are nondimensional, Equation 31 becomes

$$\frac{\partial}{\partial t^{\dagger}}A^{\dagger} + \frac{\partial}{\partial x^{\dagger}}\left((1 - \alpha A^{\dagger})A^{\dagger}\right) = \frac{\varepsilon L\hat{S}_0}{\left(U_j - 2\alpha A_{00}\right)^2} + 0.1\frac{(\Delta x^{\dagger})^2}{\Delta t^{\dagger}}\frac{\partial^2 A^{\dagger}}{\partial x^{\dagger 2}}. \tag{34}$$

Note that A_{00} is the average value of $\hat{A}$ (a constant). Apart from the (small) diffusion term, the properties of $A^{\dagger}$ are governed by α and $\varepsilon \,/\, \left(U_j - 2\alpha A_{00}\right)^2$ for a fixed $\hat{S}_0$ and L. This explains, for example, the opposing behaviors of LWA in response to ε and U_j in Figures 11 and 12.

6. Two-Layer Model

The foregoing 1D model allows one to test the sensitivity of probability distributions of LWA to external model parameters. In reality, these parameters are determined by the internal dynamics of the atmosphere, together with boundary conditions and other climate forcings. For one, the speed of the jet in the upper troposphere is influenced by meridional temperature gradients, surface friction, and momentum transport by eddies and mean meridional circulations. A major source for transient eddy forcing is upstream cyclogenesis (Colucci, 1985), which in turn is influenced by temperature gradients and meridional eddy heat flux at low levels. In all likelihood, factors that control the LWA distribution are not mutually independent, and this complicates the projection of the trend in the frequency of extreme events under climate change. An active debate concerns whether the reduction in the meridional temperature gradients due to polar amplification leads to more anomalous jet behaviors in the midlatitudes (Francis et al., 2017).

Here we explore this question by examining the LWA distributions produced by quasigeostrophic two-layer model (Phillips, 1951). To isolate the role of interaction between transient eddy and flow, we do not impose stationary waves. As in many previous studies utilizing this model, the flow is relaxed to a baroclinically unstable, zonally symmetric "radiative equilibrium" state (e.g., Esler, 1998). Eddies emerge from baroclinic instability and interact with the zonal flow in a much more realistic fashion than in the 1D model. We set up the model domain as a 28,000 km × 28,000 km rectangular channel, periodic in x (longitude) and bounded in y at north and south ends. We choose $y = 0$ to be the center latitude of the channel, that is, the boundaries are at $y = \pm 14000$ km. The two layers have an equal rest thickness D with a flat bottom, and the internal Rossby radius ($L_D \equiv \sqrt{g'D} \,/\, f_0$; g' is reduced gravity and f_0 is the Coriolis parameter) is assumed to be 800 km. Consistent with Earth's midlatitudes, we assume $\beta = 1.6 \times 10^{-11}$ m^{-1}s^{-1}. The model is solved with a 2D spectral transform method, with nonlinear terms evaluated on 256 × 256 grids in physical space. Governing equations are split into eddy QGPV and the zonal-mean QGPV gradient to accommodate different boundary conditions at the rigid walls. Both quantities are subject to radiative relaxation with a timescale of $\tau_{\mathrm{RAD}} = 30$ days and Ekman damping (applied only to relative vorticity in the lower layer) with a timescale $\tau_{\mathrm{FRIC}} = 5$ days. We also add 6th-order hyperviscosity $\nu = 2.97 \times 10^{24}$ m^6 s^{-1} to suppress small-scale noise.

In the zonal mean (denoted by square bracket), vertical shear (the difference in the zonal winds between the two layers) $[u_1] - [u_2]$ is relaxed toward the radiative equilibrium profile

$$\Delta U_{\mathrm{E}}(y) = \Lambda \,\mathrm{sech}^2\left(y/3L_D\right). \tag{35}$$

Through thermal wind balance, this represents meridional temperature gradients concentrated to the center of the channel. The shear parameter Λ in Equation 35 thus controls the north-south thermal contrast across the jet (i.e., available potential energy) and affects baroclinic eddy activity. The above choice of ΔU_{E} ensures that baroclinic eddies remain in the center of the channel so the side boundaries will not affect our results adversely. (We have tested different profiles of ΔU_{E} and found that the results remain qualitatively similar as long as the jet is meridionally isolated.) Since the lower-layer wind $[u_2]$ is relaxed toward 0 by friction, the upper-layer wind $[u_1]$ is relaxed toward ΔU_{E}. We will vary Λ in the subsequent experiments. The model is initialized with a meridionally symmetric, small-amplitude white noise, superposed on the zonally symmetric radiative equilibrium state $\left([u_1] = \Delta U_{\mathrm{E}}, [u_2] = 0\right)$. We run the model for 3 years and sample the upper-layer QGPV every 3.3 h after a statistical steady state is reached. The subsequent analysis focuses on the upper layer, which represents the upper troposphere in the midlatitudes where the jet is most prominent. The analyses will be presented for $y = 0$, the mean location of the jet axis, because we are interested in the disruptions of the jet by the waves moving along the stream. However, baroclinic waves also radiate meridionally, and as they break at the flanks of the jet, large wave activity tends to occur more often in the critical layers than at the axis of the jet.

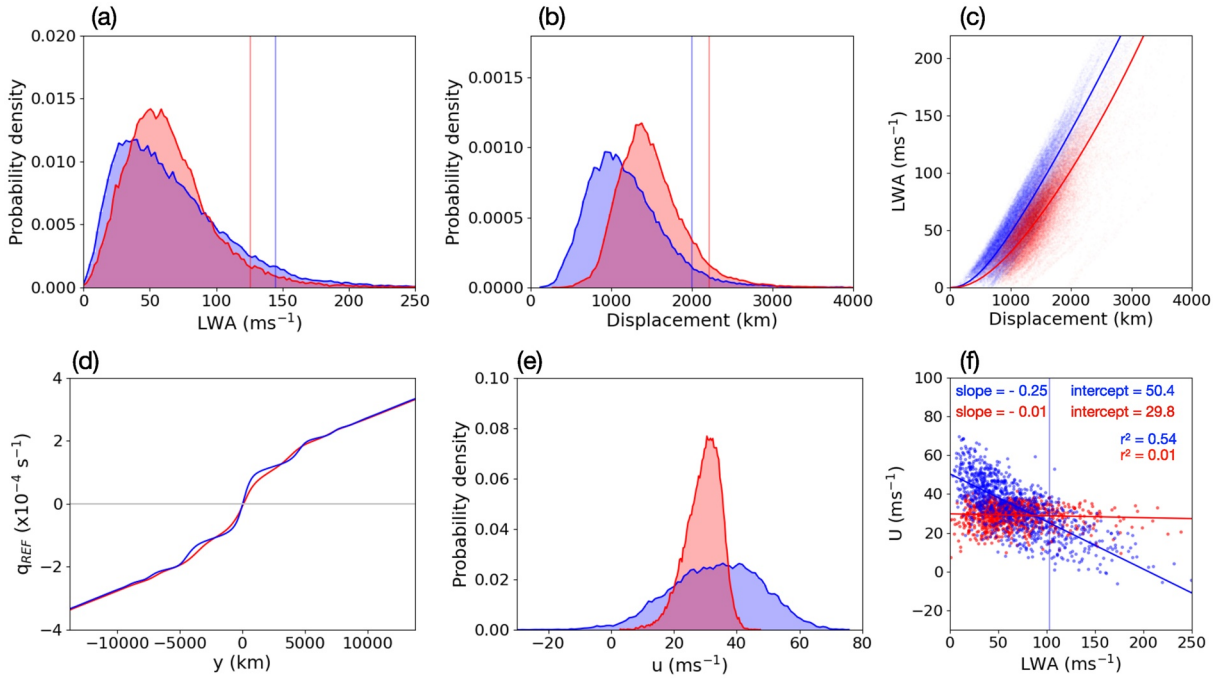

Figure 13. Properties of the two-layer quasigeostrophic model experiments with $\Lambda = 30\,\mathrm{ms}^{-1}$ (blue) and the run with the same Λ but without nonlinear zonal flux of quasigeostrophic potential vorticity (QGPV) (red). (a) Probability distribution of 4-day averaged total LWA, sampled from all grid points at the center of the top layer $(y = 0)$ after day 155 (sample size = 61,696). Vertical lines indicate 95 percentile marks. (b) As in (a) but for total displacement $(\Delta y_C + \Delta y_A)$. (c) Relationship between total displacement (abscissa) and total local wave activity (LWA) (ordinate) at $y = 0$. Both quantities are averaged over 4 days. The curve fits are based on scaling of Equation 8 + Equation 9. (d) Meridional profiles of q_{REF} in the upper layer, averaged between day 155 and 1091. (e) Probability distribution of 4-day averaged u, sampled as in (a). (f) Scatter diagram of total LWA (abscissa) versus zonal flow u (ordinate) at the center of the top layer $(y = 0)$. Each data point represents an average over 4 days and one quarter of the channel length, between days 155 and 1091. Also shown are linear regression with the slope, intercept and the r^2 values indicated in the panel. The thin vertical line indicates the threshold value Equation 27 for the control run based on the estimated slope α and the intercept u_0, assuming $c_g \approx 0$.

6.1. Effects of Nonlinearity on the Zonal QGPV Flux

Before varying the vertical shear, we explore the effects of nonlinearity on the distribution of LWA and zonal wind in this model. Unlike the 1D model, the two-layer model does not allow one to control the strength of nonlinearity as an external parameter, but one can suppress the pertinent nonlinear term in the governing equations and observe its effect. Specifically, we compare a full-dynamics control run with another run in which the convergence of zonal eddy QGPV flux, $-\partial(u^* q^*) / \partial x$, is artificially suppressed in the eddy QGPV equation for both layers (The asterisk denotes departure from the zonal mean.) This is done in the code by subtracting the term when all nonlinear terms are evaluated on the physical grids. This simple alteration does not affect the zonal-mean budget of QGPV but eliminates local eddy-flow interaction, in a fashion similar to suppressing the nonlinear term in the 1D model. Otherwise the two runs are identical. Here we use $\Lambda = 30\,\mathrm{ms}^{-1}$ for both runs.

Figures 13a and 13b compare, respectively, the probability distributions of the upper-layer LWA and displacement for the two runs at the center of the channel $(y = 0)$ after the model has reached a statistical steady state. Since the statistics of cyclonic and anticyclonic displacements are nearly identical due to the symmetry of the flow, we lump together cyclonic and anticyclonic displacements and LWA. The distributions for the control run resemble Figure 6, except LWA is more positively skewed due to the lack of stationary waves. The altered run deviates from the control run in two ways. First, the displacement is systematically higher (Figure 13b) and second, for a given displacement the corresponding LWA is systematically lower (Figure 13c). This last difference arises from distinct gradients in q_{REF} near the center of the channel (Figure 13d) due to different mixing characteristics of the two runs. The two aspects of the altered run have competing effects on the LWA distribution, and consequently the mean and the overall range of

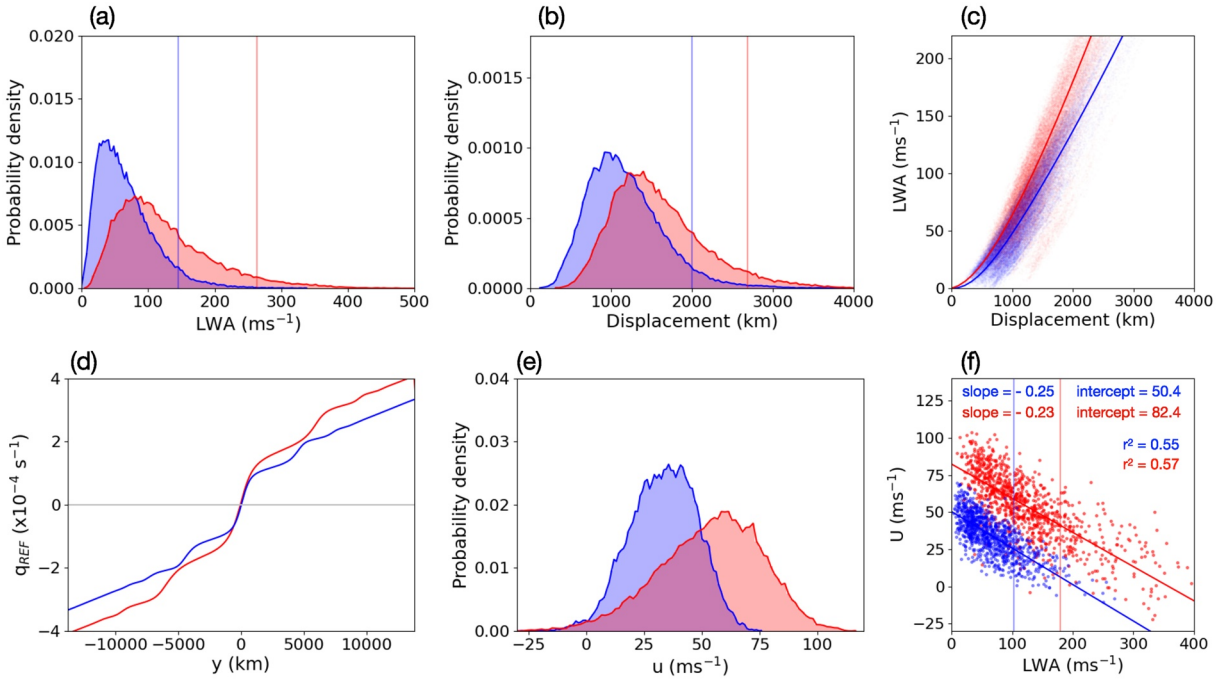

Figure 14. As in Figure 13 but for runs with $\Lambda = 30\,\mathrm{ms}^{-1}$ (blue) and $50\,\mathrm{ms}^{-1}$ (red). Both experiments are done with full dynamics.

LWA distribution is similar to the control run (Figure 13a). However, there is a discernible difference in the shape of LWA distributions between the two experiments. For the run without the nonlinear flux, the mode is shifted to the right and the peak is higher, whereas probability is suppressed at small and large values of LWA (Figure 13a). Nonlinearity in the control run spreads the distribution more to small- and large-wave events. For example, the 95 percentile value of LWA is 145 ms^{-1} for the control run but 126 ms^{-1} for the altered run.

While the difference in the LWA distributions in Figure 13a is modest, the same is not true in the distribution of the zonal wind (Figure 13e). The variance of the zonal wind along the jet axis is vastly reduced in the altered run, and the mean value is also a little smaller. In particular, occurrences of negative values (easterly winds in 4-day average) are virtually eliminated, whereas in the control run they stand 1.4 percent of chance. Therefore, there is hardly any disruption of the jet stream in the altered run even with large LWA. This is further substantiated in the covariance plot of LWA and u in Figure 13f. The control run shows a clear negative covariance between LWA and u, whereas it is altogether absent in the altered run. Removal of the nonlinear zonal QGPV flux thus eliminates local eddy-flow interaction, and large wave events are not associated with a weakened jet. The nearly flat red line gives $\alpha \sim 0.01$ and the required threshold LWA [Equation 27, assuming $c_g \approx 0$] ~1500 ms^{-1}, so there is no chance for the jet to be disrupted through the "traffic jam" mechanism. In the control run, on the other hand, LWA is above the threshold~101 (ms^{-1}) about 18 percent of the time (Yet only a small fraction of these large LWA events leads to a reversal of the jet, as it requires a sustained eddy forcing).

6.2. Dependence on Shear

Now we examine the effects of shear (meridional temperature gradient) on the distribution of LWA and u. Figure 14 compares the control run in the preceding subsection with another run with a greater shear ($\Lambda = 50\,\mathrm{ms}^{-1}$, with full dynamics) for the same location ($y = 0$ in the upper layer). The high-shear run shifts the LWA distribution to higher values relative to the control run (Figure 14a). This shift is primarily due to enhanced displacements (Figure 14b). Although LWA for a given displacement also increases (Figure 14c) because of the difference in q_{REF} (Figure 14d), this effect proves relatively minor as we will see below. For

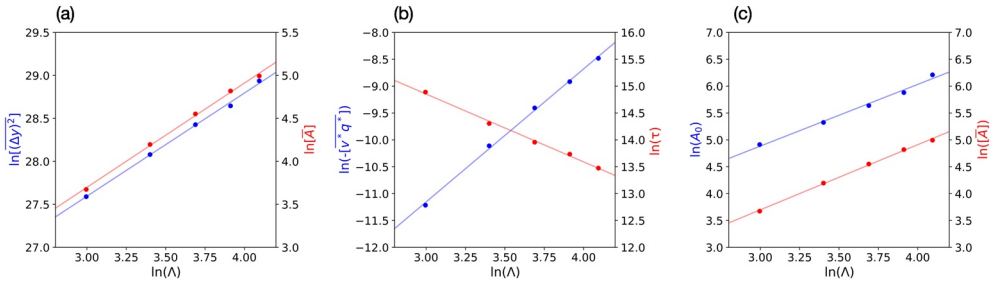

Figure 15. (a), (b): Dependence of terms in Equation 40, measured at $y = 0$ in the upper layer, as functions of shear (logarithm of Λ). (a) ln Λ (abscissa) versus $\ln[\bar{A}]$ (red) and $\ln[\overline{(\Delta y)^2}]$ (blue). Where Δy involves positive and negative displacements simultaneously, their respective squares are summed. Slopes of the fitted lines are 1.21 (red) and 1.20 (blue). The five points correspond to $\Lambda = 20$, 30, 40, 50, and 60 ms^{-1}. (b) As in (a) but for $\ln(-[\overline{v^* q^*}])$ (blue, slope = 2.48) and $\ln \tau$ (red, slope = −1.26). The time average was taken between days 155–1091. (c) ln Λ (abscissa) versus $\ln[\bar{A}]$ (red, slope = 1.21) and $\ln A_0$ (blue, slope = 1.15), where A_0 is LWA that corresponds to zero u. See text for details.

the high-shear run, the distribution of 4-day averaged u is stretched to higher values (Figure 14e) because the upper-layer flow is relaxed toward ΔU_E, proportional to shear [Equation 35]. Yet, u still turns negative (easterly) about 1.4 percent of the time, the same fraction as the control run. The reversal of the jet is invariably accompanied by large LWA. Figure 14f shows that LWA and u covary in a similar way to the control run with a nearly identical slope, but for the same LWA the corresponding u is significantly higher. Therefore, to reverse the zonal wind, one needs much larger LWA.

While the shifts in the mean speed of the jet is directly related to shear through Equation 35, those in the mean local wave activity (LWA) are related to the changes in eddy forcing and damping. In the upper layer, the zonal-mean LWA is governed by

$$\frac{\partial [A]}{\partial t} = [-v^* q^*] - \frac{[A]}{\tau}, \tag{36}$$

where the square bracket and asterisk denote the zonal average and departure from it, respectively, and τ is damping time scale associated with radiative forcing and mixing. Equation 36 is analogous to the zonal mean of Equation 10 with Equation 17. After time averaging (denoted by an overbar), the budget is balanced between eddy forcing and damping of LWA (Nakamura & Zhu, 2010, their Equation 24a):

$$\left[\bar{S}\right] - \frac{[\bar{A}]}{\tau} = 0, \qquad [\bar{S}] = [-\overline{v^* q^*}] > 0. \tag{37}$$

Note that the eddy QGPV flux is generally downgradient and since the mean gradient is positive, $[\overline{v^* q^*}] < 0$. Equation 37 is analogous to Equation 29 for the 1D model. If we use the linear approximation to wave activity, $[\bar{A}] \approx (1/2)(\partial q_{\mathrm{REF}} / \partial y)[\overline{(\Delta y)^2}]$, then Equation 37 may be arranged into

$$[\bar{A}] \approx \frac{1}{2} \frac{\partial q_{\mathrm{REF}}}{\partial y} [\overline{(\Delta y)^2}] \approx [-\overline{v^* q^*}]\tau. \tag{38}$$

For a slightly different value of shear, the above balance will be achieved at a different value. Denoting the change in each term in Equation 38 by δ,

$$\delta[\bar{A}] \approx \delta\left(\frac{1}{2} \frac{\partial q_{\mathrm{REF}}}{\partial y} [\overline{(\Delta y)^2}]\right) \approx \delta\left([-\overline{v^* q^*}]\tau\right). \tag{39}$$

After applying the chain rule to Equation 39 and dividing by Equation 38, we obtain

$$\underbrace{\delta \ln\left[\bar{A}\right]}_{(\mathrm{i})} \approx \underbrace{\delta \ln\left[\overline{(\Delta y)^2}\right]}_{(\mathrm{ii})} + \underbrace{\delta \ln\left(\frac{\partial q_{\mathrm{REF}}}{\partial y}\right)}_{(\mathrm{iii})} \approx \underbrace{\delta \ln\left[-\overline{v^* q^*}\right]}_{(\mathrm{iv})} + \underbrace{\delta \ln \tau}_{(\mathrm{v})}. \tag{40}$$

Equation 40 shows that changes in the mean wave activity may be broken down in two different ways: changes in the displacement and the QGPV gradient, and changes in the eddy forcing and the damping

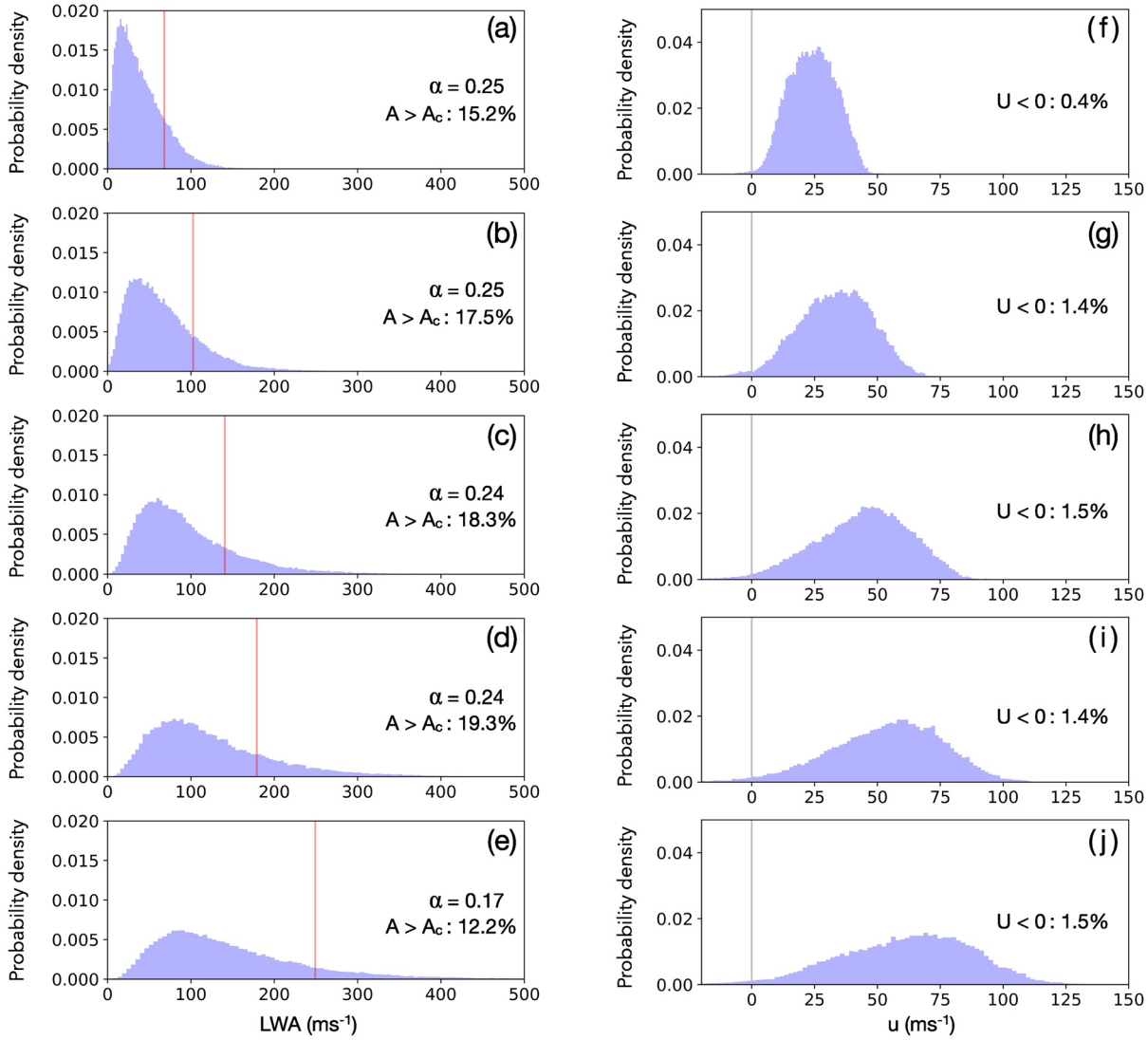

Figure 16. Left column [(a)–(e)]: Probability densities of 4-day averaged LWA in the top layer at $y = 0$ for wind shear $\Lambda = 20$, 30,40, 50 and 60 ms^{-1}. Data are sampled at all grid points during a 3-year run after a statistical steady state is reached. Vertical line denotes blocking threshold for each model run, calculated as $u_0 / (2\alpha)$, where u_0 and α are the y-intercept and the magnitude of slope in the regression of local wave activity (LWA) and u for the top layer (see Figure 14f). Percentage indicates the fraction of the periods in which the 4-day averaged LWA surpassed the threshold. Right column [(f)–(j)]: As in (a)–(e) but for the zonal wind u. Percentage indicates the fraction of the periods in which the 4-day averaged u is negative (easterly).

timescale. Figure 15 plots various terms in Equation 40 for five values of shear Λ (20, 30, 40, 50, and 60 ms^{-1}), expressed in terms of natural logarithm of Λ. Figure 15a compares the dependence of terms (i) and (ii) on natural logarithm of shear. These terms fall on lines of nearly identical slopes, suggesting that changes in the mean LWA [term (i)] is almost entirely due to changes in the displacement [term (ii)], and changes in the gradient of q_{REF} [term (iii)] play a negligible role. However, the slope is greater than 1 (1.20–1.21), meaning that the rate of change of LWA is greater than that of shear. Meanwhile, Figure 15b shows that an increasing shear increases eddy QGPV flux [term (iv)] through enhanced baroclinic instability, but it also decreases damping time [term (v)] through enhanced mixing. While the eddy QGPV flux increases at a rate 2.48 times greater than that of shear, about half of it is compensated by the decreased damping time. Taken together, an increasing shear enhances the mean wave activity by enhancing the *net* eddy forcing, that is, the surplus of eddy QGPV flux over damping by mixing, which also enhances meridional displacements.

Figure 16 shows probability distributions of 4-day averaged LWA and u at $y = 0$ in the upper layer, varying Λ from 20 to 60 ms^{-1}. As Λ increases, high values of LWA become more common and extreme LWA values increase, essentially flattening the distributions. Meanwhile, the estimated threshold of the jet disruption also increases with shear, keeping the portion of the LWA distribution surpassing the threshold largely unchanged. Between $\Lambda = 20$ and 50 ms^{-1}, that percentile stays in the range of 15–19 (Figures 16a–16d). The corresponding distributions of u are negatively skewed, and the distribution also flattens with an increasing Λ as large values become more dominant. However, there is always a small portion of u below zero, that is, easterly, and this fraction is remarkably steady (~1.5 percent). Thus, higher (lower) values of shear do not necessarily imply higher or lower probability of jet disruptions, confirming the analysis of Figure 14. The enhanced eddy forcing and LWA that would otherwise promote the disruption of the jet compete with the increased jet speed that resists the disruption. The competition keeps the frequency of jet disruptions insensitive to vertical shear (meridional temperature gradient). This sends a caveat to the interpretation of the 1D model when eddy forcing and the speed of the jet are varied independently, while in reality they are likely to covary through shear, so their effects largely cancel.

Another way to see this is to assume that $u \approx u_0 - \alpha A$ in the upper layer [as in the 1D model Equation 23]. Then u is negative for $A > u_0 / \alpha \equiv A_0$. If the value of A_0 and the distribution of A both scale similarly with shear, the fraction of $A > A_0$ (i.e., probability of zonal wind reversal) will be independent of shear. Figure 15c shows A_0 computed from the slope and intercept of the line fitted to the LWA-u relation at $y = 0$ as a function of shear (blue line). The slope of this line is close to the slope of the mean LWA (red), suggesting that A_0 (primarily determined by the jet speed) and the entire distribution of A (primarily determined by the eddy forcing) indeed share a common scaling with shear.

7. Summary and Conclusions

LWA is a fundamental measure of the amplitude of Rossby waves and waviness of the jet stream. Large values of LWA are often associated with block-related weather anomalies (Figure 5). Unlike other metrics of eddy amplitude, LWA obeys a relatively simple budget that is evaluable with data. In this article we have analyzed the observed probability distributions of column LWA in the midlatitudes and explored processes that control them. LWA is partitioned into cyclonic and anticyclonic contributions and further recast in terms of the reference-state QGPV, q_{REF}, and its meridional displacement [Equations 8 and 9]. The distributions of displacement and those of LWA are therefore related through q_{REF} (Figure 6). In the midlatitudes the observed distribution of LWA (particularly its cyclonic or anticyclonic component) is positively skewed. LWA and its seasonal and intraseasonal variance are generally greater in the NH than in the SH. Anticyclonic displacements are greater than cyclonic displacements in the NH, but the asymmetry varies with season and location (Figure 4).

In the midlatitudes LWA primarily propagates eastward along the jet stream. Using the 1D traffic flow model (NH18, P19) driven by transient eddy forcing with the observed spectra, we have shown that the model is capable of reproducing the observed LWA distribution qualitatively. Most importantly, even though the transient eddy forcing is symmetrically distributed, skewness arises in the distribution of LWA from nonlinearity in its zonal advection. The nonlinearity reflects the negative covariance between LWA and the zonal wind: the wavier the jet stream, the slower its eastward component (Figure 8). A locally slowed jet stream promotes stagnation and further pileup of LWA. This feedback is analogous to the relationship between the traffic density and traffic speed on a highway, and when a threshold is exceeded, it leads to a quick formation of a "traffic jam" or disruption of the jet stream (NH18). That both the positive skew and block-producing extreme values in the LWA distribution stem from nonlinearity in the *zonal* advection paints a much simpler picture than for the non-Gaussian distribution of surface temperature, whose skewness involves both signs and is influenced by 2D advection (Garfinkel & Harnik, 2017; Linz et al., 2018). In fact, to the extent that LWA governs the large-scale dynamics of the atmosphere in the midlatitudes, we suspect that at least some extreme values of surface temperatures are linked to nonlinear zonal advection of LWA.

It is also found that increasing transient and stationary eddy forcings and decreasing the jet speed in the 1D model all make the LWA distribution broader and thus increase the probability of threshold crossing and jet disruptions (Figure 12). However, some of these parameters are mutually dependent in the real atmosphere.

Subsequent experimentation with the two-layer model shows that transient eddy forcing and the jet speed both increase with an increasing vertical shear, and their opposing tendencies in shifting the LWA probability leave the frequency of threshold crossing and jet disruptions largely unaltered with shear (Figure 16). An earlier work by Hassanzadeh et al. (2014) also examined blocking frequency while changing the surface temperature gradient in a dry GCM. They report that a decreasing temperature gradient diminishes both eddy activity and the jet speed, although the frequency of blocking in their study also decreases according to their metric based on geopotential height. In a related study, Xue et al. (2017) apply a variant of LWA (Chen et al., 2015) to reanalysis and model simulations and conclude that the statistics of total LWA in the boreal midlatitudes do not change appreciably in response to the reduced meridional temperature gradient associated with the Arctic amplification (They instead find an increase in anticyclonic LWA over the northern Eurasia.) The model design in the present study does not include asymmetry between anticyclonic and cyclonic LWA, but the role of the warming Arctic in selective reinforcement of anticyclonic wave activity is worth further investigation.

There is a similarity between the present work and the vertical transmission of Rossby waves in the winter stratosphere. Temperature distributions in the winter stratosphere are known to have a positive skew (Labitzke, 1982; Gillett et al., 2001; Yoden et al., 2002). Watt-Meyer and Kushner (2018) explain this in terms of interference between linear and nonlinear parts of upward wave activity flux. We may draw an analogy and postulate that skewness in the tropospheric LWA distribution may be also explained by the interference between the linear and nonlinear wave activity flux in the zonal. This is hinted, for example, in Figure 13a where after removing the nonlinear zonal flux of QGPV the LWA distribution becomes less asymmetric. However, interference is probably half the story–the feedback through eddy-flow interaction augments large values of LWA and rapid deceleration of the zonal wind, reinforcing the probability of jet disruptions. Midlatitude weather anomalies involving local reversal of the jet stream are unlikely to arise without this feedback. Similarly, the same feedback is also likely at play in the stratosphere (Nakamura et al., 2020) and partially responsible for the skewed distribution of stratospheric temperatures.

Work is underway to delineate more detailed evolution of LWA budget during observed large wave events that involve jet disruptions.

Appendix A: 1D Model Setup

The 1D model used in this article discretizes Equation 25 on a periodic channel of length $L = 28000$ km with 1,000 equally spaced grids in x ($\Delta x = 28$ km). A 3rd-order Adams-Bashforth scheme (Durran, 1991) is used to integrate the equation in time with a time increment of $\Delta t = 120$ s. Small numerical diffusion with a diffusion coefficient $\kappa \equiv 0.1\Delta x^2 / \Delta t$ is added. The forcing spectra (20 wavenumbers × 120 frequencies) are imported at the beginning of integration, and each wave component is assigned a random phase before the integration. While the model is inexpensive to run, the majority of calculation is spent in the reconstruction of transient eddy forcing $\hat{S}_0$ from the superposition of 2,400 waves at each time step. Each experiment is run for 933 days (600,000 time steps) with the transient eddy forcing, and the data are saved every 6 h. We repeat the experiment six times, each time randomizing the phase of the forcing functions. Probability distribution is constructed by sampling 4-day averaged LWA at all longitude grids. The ensemble-mean distribution typically converges after 3–4 iterations.

Acknowledgments
The bulk of this work has been conducted as CV's honors thesis at the Department of the Geophysical Sciences, University of Chicago, and supported by NSF Grant AGS1909522. Technical assistance by Clare Huang and Pragallva Barpanda and resources at Research Computing Center at the University of Chicago are gratefully acknowledged. The authors thank three anonymous reviewers whose conscientious critiques helped improve the presentation of this paper.

Data Availability Statement

ERA-Interim reanalysis data may be downloaded from https://apps.ecmwf.int/datasets/data/interim-full-daily/levtype=sfc/. The python code to compute LWA is found here: https://github.com/csyhuang (2016_falwa). The 1D model of LWA may be downloaded from https://github.com/clairevalva/LWA-1D.

References

Chang, E. K. M. (1993). Downstream development of baroclinic waves as inferred from regression-analysis. *Journal of the Atmospheric Sciences*, *50*, 2038–2053. https://doi.org/10.1175/1520-0469(1993)050<2038:ddobwa>2.0.co;2

Chen, G., Lu, J., Burrows, D. A., & Leung, L. R. (2015). Local finite-amplitude wave activity as an objective diagnostic of midlatitude extreme weather. *Geophysical Research Letters*, *42*, 10952–10960. https://doi.org/10.1002/2015gl066959

Colucci, S. J. (1985). Explosive cyclogenesis and large-scale circulation changes - Implications for atmospheric blocking. *Journal of the Atmospheric Sciences*, *42*, 2701–2717. https://doi.org/10.1175/1520-0469(1985)042<2701:ecalsc>2.0.co;2

Colucci, S. J. (2001). Planetary-scale preconditioning for the onset of blocking. *Journal of the Atmospheric Sciences*, *58*, 933–942. https://doi.org/10.1175/1520-0469(2001)058<0933:PSPFTO>2.0.CO;2

Dee, D. P., Uppala, S. M., Simmons, A. J., Berrisford, P., Poli, P., Kobayashi, S., et al. (2011). The ERA-Interim reanalysis: Configuration and performance of the data assimilation system. *Quarterly Journal of the Royal Meteorological Society*, *137*, 553–597. https://doi.org/10.1002/qj.828

Durran, D. R. (1991). The 3rd-order adams-bashforth method - An attractive alternative to leapfrog time differencing. *Monthly Weather Review*, *119*, 702–720. https://doi.org/10.1175/1520-0493(1991)119<0702:TTOABM>2.0.CO;2

Edmon, H. J., Hoskins, B. J., & McIntyre, M. E. (1980). Eliassen-Palm cross setions for the troposphere. *Journal of the Atmospheric Sciences*, *37*, 2600–2616. https://doi.org/10.1175/1520-0469(1980)037<2600:EPCSFT>2.0.CO;2

Esler, J. (1998). The turbulent equilibration of an unstable baroclinic jet. *Journal of Fluid Mechanics*, *599*, 241–268. https://doi.org/10.1017/s0022112008000153

Francis, J. A., Vavrus, S. J., & Cohen, J. (2017). Amplified Arctic warming and mid-latitude weather: New perspectives on emerging connections. *Wiley Interdisciplinary Reviews-Climate Change*, *8*. https://doi.org/10.1002/wcc.474

Garcia-Herrera, R., Diaz, J., Trigo, R. M., Luterbacher, J., & Fischer, E. M. (2010). A review of the European summer heat wave of 2003. *Critical Reviews in Environmental Science and Technology*, *40*, 267–306. https://doi.org/10.1080/10643380802238137

Garfinkel, C. I., & Harnik, N. (2017). The non-Gaussianity and spatial asymmetry of temperature extremes relative to the storm track: The role of horizontal advection. *Journal of Climate*, *30*, 445464. https://doi.org/10.1175/JCLI-D-15-0806.1

Ghinassi, P., Baumgart, M., Teubler, F., Riemer, M., & Wirth, V. (2020). A budget equation for the amplitude of Rossby wave packets based on finite-amplitude local wave activity. *Journal of the Atmospheric Sciences*, *77*, 277–296. https://doi.org/10.1175/jas-d-19-0149.1

Gillett, N. P., Baldwin, M. P., & Allen, M. R. (2001). Evidence for nonlinearity in observed stratospheric circulation changes. *Journal of Geophysical Research-Atmospheres*, *106*, 7891–7901. https://doi.org/10.1029/2000jd900720

Hassanzadeh, P., Kuang, Z. M., & Farrell, B. F. (2014). Responses of midlatitude blocks and wave amplitude to changes in the meridional temperature gradient in an idealized dry GCM. *Geophysical Research Latters*, *41*, 5223–5232. https://doi.org/10.1002/2014gl060764

Huang, C. S. Y., & Nakamura, N. (2016). Local finite-amplitude wave activity as a diagnostic of anomalous weather events. *Journal of the Atmospheric Sciences*, *73*(1), 211–229. https://doi.org/10.1175/JAS-D-15-0194.1

Huang, C. S. Y., & Nakamura, N. (2017). Local wave activity budgets of the wintertime northern hemisphere: Implication for the Pacific and Atlantic storm tracks. *Geophysical Research Letters*, *44*, 5673–5682. https://doi.org/10.1002/2017GL073760

Labitzke, K. (1982). On the interannual variability of the middle stratosphere during the northern winters. *Journal of the Meteorological Society of Japan*, *60*, 124–139. https://doi.org/10.2151/jmsj1965.60.1_124

Linz, M., Chen, G., & Hu, Z. (2018). Large-scale atmospheric control on non-Gaussian tails of midlatitude temperature distributions. *Geophysical Research Letters*, *45*, 91419149. https://doi.org/10.1029/2018GL079324

Luo, D.-H. (2005). Barotropic envelope Rossby soliton model for block-eddy interaction. part i: Effect of topography. *Journal of the Atmospheric Sciences*, *62*, 5–21. https://doi.org/10.1175/1186.1

Luo, D.-H., Zhang, W. Q., Zhong, L. H., & Dai, A. G. (2019). A nonlinear theory of atmospheric blocking: A potential vorticity gradient view. *Journal of the Atmospheric Sciences*, *76*, 2399–2427. https://doi.org/10.1175/jas-d-18-0324.1

Mullen, S. L. (1987). Transient eddy forcing of blocking flows. *Journal of the Atmospheric Sciences*, *44*, 3–22. https://doi.org/10.1175/1520-0469(1987)044<0003:tefobf>2.0.co;2

Nakamura, H. (1994). Rotational evolution of potential vorticity associated with a strong blocking flow configuration over Europe. *Geophysical Research Letters*, *21*, 2003–2006. https://doi.org/10.1029/94GL01614

Nakamura, H., & Wallace, J. M. (1993). Synoptic behavior of baroclinic eddies during the blocking onset. *Monthly Weather Review*, *121*, 1892–1903. https://doi.org/10.1175/1520-0493(1993)<121h1892:sbobedi>2.0.co;2

Nakamura, N., Falk, J., & Lubis, S. W. (2020). Why are stratospheric sudden warmings sudden (and intermittent)? *Journal of the Atmospheric Sciences*, *77*, 943–964. https://doi.org/10.1175/jas-d-19-0249.1

Nakamura, N., & Huang, C. S. Y. (2017). Local wave activity and the onset of blocking along a potential vorticity front. *Journal of the Atmospheric Sciences*, *74*, 2341–2362. https://doi.org/10.1175/jas-d-17-0029.1

Nakamura, N., & Huang, C. S. Y. (2018). Atmospheric blocking as a traffic jam in the jet stream. *Science*, *361*(6397), 42–47. https://doi.org/10.1126/science.aat0721

Nakamura, N., & Solomon, A. (2010). Finite-amplitude wave activity and mean flow adjustments in the atmospheric general circulation. Part I: Quasigeostrophic theory and analysis. *Journal of the Atmospheric Sciences*, *67*, 3967–3983. https://doi.org/10.1175/2010jas3503.1

Nakamura, N., & Zhu, D. (2010). Finite-amplitude wave activity and diffusive flux of potential vorticity in eddy-mean flow interaction. *Journal of the Atmospheric Sciences*, *67*, 2701–2716. https://doi.org/10.1175/2010jas3432.1

Naoe, H., Matsuda, Y., & Nakamura, H. (1997). Rossby wave propagation in idealized and realistic zonally varying flows. *Journal of the Meteorological Society of Japan*, *75*, 687–700. https://doi.org/10.2151/jmsj1965.75.3_687

Narinesingh, V., Booth, J., Clark, S. K., & Ming, Y. (2020). Atmospheric blocking in an aquaplanet and the impact of orography. *Weather and Climate Dynamics*, *1*, 293–311. https://doi.org/10.5194/wcd-1-293-2020

Paradise, A., Rocha, C. B., Barpanda, P., & Nakamura, N. (2019). Blocking statistics in a varying climate: Lessons from a "traffic jam" model with pseudostochastic forcing. *Journal of the Atmospheric Sciences*, *76*, 3013–3027. https://doi.org/10.1175/jas-d-19-0095.1

Phillips, N. A. (1951). A simple 3-dimensional model for the study of large-scale extratropical ow patterns. *Journal of Meteorology*, *8*, 381–394. https://doi.org/10.1175/1520-0469(1951)008<0381:astdmf>2.0.co;2

Plumb, R. A. (1985). On the three-dimensional propagation of stationary waves. *Journal of the Atmospheric Sciences*, *42*, 217–229. https://doi.org/10.1175/1520-0469(1985)042h<0217:OTTDPOi>2.0.CO;2

Plumb, R. A. (1986). Three-dimensional propagation of transient quasi-geostrophic eddies and its relationship with the eddy forcing of the time-mean ow. *Journal of the Atmospheric Sciences*, *43*, 1657–1678. https://doi.org/10.1175/1520-0469(1986)043<1657:TDPOTQ>2.0.CO;2

Shaw, T., Baldwin, M., Barnes, E., Caballero, R., Garfinkel, C. I., Hwang, Y.-T., et al. (2016). Storm track processes and the opposing influences of climate change. *Nature Geoscience*, *9*, 656–664. https://doi.org/10.1038/ngeo2783

Takaya, K., & Nakamura, H. (2001). A formulation of a phase-independent wave activity flux for stationary and migratory quasigeostrophic eddies on a zonally varying basic flow. *Journal of the Atmospheric Sciences*, *58*, 608–627. https://doi.org/10.1175/1520-0469(2001)058<0608:AFOAPI>2.0.CO;2

Wang, L., & Nakamura, N. (2016). Covariation of finite-amplitude wave activity and the zonal-mean flow in the midlatitude troposphere. Part II. eddy forcing spectra and the periodic behavior in the southern hemisphere summer. *Journal of the Atmospheric Sciences*, *73*, 4731–4752. https://doi.org/10.1175/jas-d-16-0091.1

Watt-Meyer, O., & Kushner, P. J. (2018). Why are temperature and upward wave activity flux positively skewed in the polar stratosphere? *Journal of Climate*, *31*, 115–130. https://doi.org/10.1175/jcli-d-17-0155.1

Wirth, V., Riemer, M., Chang, E. K. M., & Martius, O. (2018). Rossby wave packets on the midlatitude waveguide—A review. *Monthly Weather Review*, *146*, 1965–2001. https://doi.org/10.1175/mwr-d-16-0483.1

Woollings, T., Barriopedro, D., Methven, J., Son, S. W., Martius, O., Harvey, B., et al. (2018). Blocking and its response to climate change. *Current Climate Change Reports*, *4*(3), 287–300. https://doi.org/10.1007/s40641-018-0108-z

Xue, D. K., Lu, J., Sun, L. T., Chen, G., & Zhang, Y. C. (2017). Local increase of anticyclonic wave activity over northern Eurasia under amplified arctic warming. *Geophysical Research Letters*, *44*, 3299–3308. https://doi.org/10.1002/2017gl072649

Yoden, S., Taguchi, M., & Naito, Y. (2002). Numerical studies on time variations of the troposphere-stratosphere coupled system. *Journal of the Meteorological Society of Japan*, *80*, 811–830. https://doi.org/10.2151/jmsj.80.811